ABSTRACT

Title of dissertation: PHYSICS-BASED AND DATA-DRIVEN MODELING OF
HYBRID ROBOT MOVEMENT ON SOFT TERRAIN

Guanjin Wang
Doctor of Philosophy, 2020

Dissertation directed by: Dr. Balakumar Balachandran
Dr. Amir Riaz
Department of Mechanical Engineering

Navigating an unmapped environment is one of the ten biggest challenges facing the robotics community. Wheeled robots can move fast on flat surfaces but suffer from loss of traction and immobility on soft ground. However, legged machines have superior mobility over wheeled locomotion when they are in motion over flowable ground or a terrain with obstacles but can only move at relatively low speeds on flat surfaces. A question to answer is as follows: If legged and wheeled locomotion are combined, can the resulting hybrid leg-wheel locomotion enable fast movement in any terrain condition?

To investigate the rich physics during dynamic interactions between a robot and a granular terrain, a physics-based computational framework based on the smoothed particle hydrodynamics (SPH) method has been developed and validated by using experimental results for single robot appendage interaction with the granular system. This framework has been extended and coupled with a multi-body

simulator to model different robot configurations. Encouraging agreement is found amongst the numerical, theoretical, and experimental results, for a wide range of robot leg configurations, such as curvature and shape.

Real-time navigation in a challenging terrain requires fast prediction of the dynamic response of the robot, which is useful for terrain identification and robot gait adaption. Therefore, a data-driven modeling framework has also been developed for the fast estimation of the slippage and sinkage of robots. The data-driven model leverages the high-quality data generated from the offline physics-based simulation for the training of a deep neural network constructed from long short-term memory (LSTM) cells. The results are expected to form a good basis for online robot navigation and exploration in unknown and complex terrains.

PHYSICS-BASED AND DATA-DRIVEN MODELING OF HYBRID ROBOT MOVEMENT ON SOFT TERRAIN

by

Guanjin Wang

Dissertation submitted to the Faculty of the Graduate School of the
University of Maryland, College Park in partial fulfillment
of the requirements for the degree of
Doctor of Philosophy
2020

Advisory Committee:
Professor Balakumar Balachandran, Chair/Advisor
Associate Professor Amir Riaz, Co-Advisor
Professor Teng Li, Department of Mechanical Engineering
Professor Amr Baz, Department of Mechanical Engineering
Professor Peter Chung, Department of Mechanical Engineering
Professor Derek Richardson, Department of Astronomy (Dean's Representative)

Acknowledgments

"Education in Chinese is Jiao Yu, where Jiao means teaching and Yu means cultivating". I appreciate my advisors Dr. Balakumar Balachandran and Dr. Amir Riaz, for their teaching inside classroom and cultivating outside classroom.

My appreciation goes to Professor Balachandran for his forming a diverse group, his vision to capture the research fashion, and his courage to explore new areas. His wisdom is like a book. When I read him, I learn what is beyond research.

I am grateful that Professor Riaz also played a very important role during my Ph.D. studies. His rich knowledge of fluid mechanics, abiding passion, and endless patience have been a great source of motivation to make me move forward.

I would like to express my sincere gratitude to Prof. Teng Li, Prof. Amr Baz, Prof. Peter Chung, and Prof. Derek Richardson not only for their kind service on my dissertation committee but also for being role models as teachers and mentors.

Many thanks also go to my peers who are like mirrors that reflect my advantages and disadvantages, which make clear the directions to make progress along and the values to keep.

Thanks to my parents for creating me. They always play a supportive role and give me the freedom to make my own decision.

Table of Contents

List of Tables

List of Figures

Chapter 1: Introduction

1.1 Motivation and Overview

Robot navigation and exploration are among the 10 grand challenges which robotics face in the next decade [1]. A vision-based navigation system embedded in the mobile robot can only help to negotiate obstacles, which are well described by geometrical features, like sharp-edged stones and rocks. Other aspects like sand, snow, and challenging terrains, are challenges for motions that robots cannot avoid during missions. Thus, designing and selecting effective gaits to navigate over terrains that may not be well describable by geometry is crucial for robot exploration.

Locomotion on natural terrain is sensitive to material properties of the substrate and the ground soil underneath which is granular material. "Can we develop a general theory of the dynamics of turbulent flows and the motion of granular materials?" is one of the 125 questions that span sciences in this century [2].

Fundamentally, granular material problems have multi-physics, multi-scale and multi-phase features. Complex and unique physical phenomena are often observed with these materials, and these phenomena have evoked the interest of researchers across a range of disciplines. From an application standpoint, granular materials are used in many engineering and commercial applications; for example,

agriculture, geo-engineering, pharmaceuticals, and energy production ([4], [5]).

1.2 Literature Review

Granular materials are ubiquitous and important as a manipulated industrial material. Most studies on granular media have focused on dry granular materials without consideration of liquid between the grains ([6]- [12]). However, wet granular materials exist in many real world problems [13].

The major effect that liquid between grains induces is the cohesion in the system. Cohesion in the wet granular system depends on the amount of liquid in the media. As indicated in Fig. 1.1, the water saturation in wet granular materials may be divided into the following four regimes as described in [14] and [45]:

• Pendular state: Capillary bridges (liquid bridge, pendular ring or meniscus) hold together granular particles when air domain is connected.

• Funicular state: Pores are either fully saturated by liquid or filled with air when pendular rings collapse on one another.

• Capillary state: All pores are filled with liquid when liquid domain is connected.

• Slurry state: Granular particles are immersed in liquid and no capillary interactions at the surface.

A small amount of liquid amongst grains can have a considerable influence on the mechanical behavior of granular matter. Due to the grain size of particles, thermal noise is omitted in consideration of particle dynamics and the interactions

Liquid Content	Saturation Regime	Schematic Diagram	Mean Forces	Physical Description
No	Dry		Gravity, contact	Cohesive stresses between grains are negligible
Small	Pendular		Gravity, contact, capillary	Cohesive forces act through Liquid bridges formed at contact points of grains
Middle	Funicular		Gravity, contact, capillary	Cohesion between particles rises from liquid bridges around the contact points and liquid-filled pores
Almost Saturated	Capillary		Gravity, contact, capillary, [drag]	Cohesive interaction is due to suction, when almost all pores are filled with the liquid. The liquid surface forms menisci and the liquid pressure is lower than the air pressure.
Saturated	Slurry		Gravity, contact, capillary, [drag]	No cohesive interaction exists between particles. The liquid pressure is not lower than the air pressure.

Figure 1.1: Granular material saturation states (adapted and revised from [14]and [45]).

between particles are taken to be dissipative. For dry granular materials, where the interstitial fluids are negligible for the particle motion, the dominant particle interactions are due to friction and collision, which are cohesionless and short range. For wet granular materials, wherein the liquid between grains are considered, the dominant interactions between grains are cohesive due to the surface tension [14]. During the collapse of wet granular material in pendular state, from experimental and numerical evidence, one can infer that due to the introduction of surface tension, the angle of repose is greater than that for a dry sand pile [15], [18].

A continuum constitutive law for granular flow would be helpful for understanding natural processes and for design and prediction of industrial processes. Through many studies, constitutive frameworks for dry granular materials have been established across geometries and regimes on the basis of theoretical, numeri-

cal and experimental efforts. To date, the rheology based constitutive law provides a unifying framework for dry dense granular flows across steady and non-steady states [19], [21]. However, there is no constitutive relationship for wet granular material in the dense flow regime.

Flow and collapse of granular materials are usually associated with large deformation and plastic failure. Approaches for solving these problems are based on either a discrete point of view or a continuum point of view. The discrete element method (DEM) is an accurate approach for granular material modeling and simulation since this method can be used to capture the discrete nature of the granular system [22]- [25]. A drawback of DEM is that it suffers from a high computational cost. Recently, meshfree methods have gained popularity. Unlike the grid-based Eulerian method, the Lagrangian nature of meshfree methods allows one to capture large deformations during granular flow and collapse without local grid distortion. Several researchers have also employed the material point method (MPM) or the smoothed particle hydrodynamics (SPH) for modeling and simulation of dry granular materials and shown the capability of these methods for studies of granular material systems [26]- [64]. To date, no SPH based computational framework has been proposed for wet granular materials. Effective locomotion on a natural terrain is important for mine detection, geo-mapping operation, and especially, extraterrestrial terrain exploration [48]. Space robots and rovers are designed to navigate in unknown and hostile terrain conditions. Obstacles that are well described by geometrical features, like sharp-edged stones and rocks, can be negotiated by using a vision-based navigation system embedded in the mobile robot, which includes a

topological representation of space together with neural networks to guide robots through an exterior space [49]. However, other aspects like sand, snow, and soft terrains, are challenges for motions that robots cannot avoid during missions. Lack of traction on a challenging terrain can result in slipping, sinkage, or even permanent immobility. Currently, unexpected sand traps are still obstacles that space rovers cannot overcome [50].

Legged locomotion has superior mobility in natural terrains over wheeled locomotion, which suffers from sinkage and slipping [50]. Legged machines use discrete footholds instead of a continuous support surface to adapt themselves to surface irregularities. Also, with the feet, one establishes contact with the ground at selected points according to the terrain conditions [51]. Another advantage of legged locomotion is the failure tolerance during static stable locomotion. With wheel locomotion, one suffers from loss of mobility, since in a locomotion mode, the wheels need to be in permanent contact with the ground [52]. However, legged machines are able to maintain a static balance and continue moving on the terrain even when one or several legs are broken.

Investigations into vehicle-terrain interactions fall in the area of terra-mechanics. The originator of this field can be said to be M. G. Bekker, who laid the foundation through his landmark work on modeling off road vehicle-soil interaction. This work has been used with attractive results over the last half-century [53]. However, classical terra-mechanics models are limited to large and heavy wheeled vehicles. Due to the occurence of sharp-edge contact, it is difficult to use classical empirical terra-mechanics analysis for the investigation of small, lightweight-wheeled vehicles
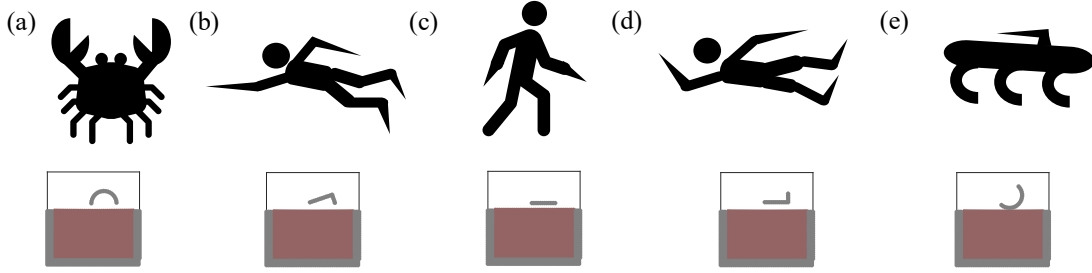
Figure 1.2: Problems of interest. The pictures in the first row are sketches of real-life examples of different leg morphologies. The figures in the second row are corresponding leg appendages studied here. (a) Crab, reversed C-leg. (b) Freestyle, reversed L-leg. (c) Human walking, flat leg (d) Backstoke, L-leg. (e) C-leg robot, C-leg.

or other bio-inspired locomotion modes, such as jumping, hopping, walking, running, and crawling [54]. Li *et al.* [48], [55] proposed the resistive force theory for the legged locomotion on granular material. From recent studies, it is known that the continuum simulations can serve as an accurate tool for simulating wheel terrain interactions with granular material at laboratory and field scales [57].

1.3   Objective and Organization

The scope of this dissertation is relevant for mobile robots used for planetary exploration, with a specific interest to provide navigation strategies through mobility evaluation of hybrid and novel locomotion systems. Furthermore, the followings are to be addressed: 1. To address the grand challenge of robot navigation on an unmapped terrain by conducting high-fidelity simulations. 2. To open up new

directions in the field of terra-mechanics and robo-physics by leveraging artificial intelligence.

Specific objectives include the following: 1. To capture the complex behavior of granular terrain by developing unified constitutive models across phases. 2.To develop a fundamental understanding of robot motion interaction with granular terrain via physics-based modeling approach to guide design of robot for effective navigation. 3.To leverage data-driven modeling approach for fast prediction of robot mobility on challenging terrain. The rest of the dissertation is organized as follows.

In Chapter 2, a grain-scale capillary interaction is introduced, as additional cohesive stress in the continuum-scale framework, to address the missing gap in continuum modeling of wet granular materials. The author coupled the visco-plastic constitutive law for dry granular material and cohesion model for wet isotropic granular material to capture the behavior of wet granular materials. This combined model is implemented in a Smoothed Particle Hydrodynamics framework because the mesh-free nature of this method can help capture the large deformation of granular flows without local grid distortion. This framework is validated by comparing numerical results with recent experimental findings for both dry and wet cases. The comparisons are illustrative of the potential of the framework to capture the behavior of granular materials across different phases. This effort can serve as a step forward in the quest for a unified continuum theory and computational framework of granular material dynamics.

In Chapter 3, to develop a high-fidelity simulator of robot moving on complex terrain to associate field test, a continuum computational framework based on the

smoothed particle hydrodynamics (SPH) method has been developed and validated by using experimental results for interactions between single robot appendages and soft terrain. This framework has been coupled with a rigid body simulator to model different robot configurations.

In Chapter 4, the author combined legged locomotion and wheeled locomotion to leverage the advantages of both locomotion modes with the aim of having a resulting hybrid leg-wheel locomotion that can enable fast motion in any terrain condition. A data-driven modeling framework has also been developed for the fast estimation of the slippage and sinkage of robots.With the data-driven model, the author has leveraged the high-quality data generated from the offline physics-based simulation for the training of a deep neural network founded on long short-term memory (LSTM) cells. The results are expected to form a good basis for online robot navigation and exploration in unknown and complex terrains.

In Chapter 5, the conclusions and future work are outlined.

Chapter 2: Solid-Like and Fluid-Like Behavior of Multi-Phase Soft Terrain

Dry granular materials have been the subject of many investigations, while wet granular materials, which widely exist in many real-world applications, have only received limited attention. The aim of this chapter [1] is to address the missing gap in continuum modeling of wet granular materials. To study the wet granular flows, a grain-scale capillary interaction is introduced, as additional cohesive stress in the continuum-scale framework. The author coupled the visco-plastic constitutive law for dry granular material and cohesion model for wet isotropic granular material to capture the behavior of wet granular materials. This combined model is implemented in a Smoothed Particle Hydrodynamics framework, since the mesh-free nature of this method can be used to capture the large deformation of granular flows without local grid distortion. The Wendland Kernel is used as the interpolation kernel to improve numerical stability. This framework is validated by comparing numerical results with recent experimental findings for both dry and wet cases. The comparisons are

---

[1] Disclosure: This chapter has been adapted from the published work, Wang, G., Riaz, A. and Balachandran, B., 2020. Smooth Particle Hydrodynamics Studies of Wet Granular Column Collapses. Acta Geotechnica, 15, pp.1205-1217.

illustrative of the potential of the framework to capture the behavior of granular materials across different phases. For different levels of friction and water content, the run-out dynamics and shear strength properties of granular materials in the final quasi-static regime are investigated. For granular flows on flat surfaces, compared with dry granular materials, with the introduction of surface tension in wet granular materials, it is found that there are increases in shear stresses locally and globally, enabling stronger internal forces to support structures with larger angles of repose. The surface energy induced cohesion is found to play an important role in low friction cases compared to high friction cases. To benchmark the numerical framework presented here, granular column collapses on curved surfaces are also investigated. For flows on curved surfaces, although there are also increases in internal shear stresses, the differences in final profiles between wet granular materials and dry granular materials are not as pronounced as that on flat surfaces due to geometric constraints. The findings of this work are demonstrative of the capabilities of the smoothed particle hydrodynamics method for the study of wet granular materials. This effort can serve as a step forward in the quest for a unified continuum theory and computational framework of granular material dynamics.

The rest of this chapter is organized as follows. In Section 2.1 and 2.2, the author has discussed the formulation used to model wet granular materials. Subsequently, in Section 2.3, the numerical implementation of the governing equations and boundary conditions in the SPH framework are addressed. In Section 2.4, comparisons are made between numerical results and experimental results available in the literature. Following that, the author has presented numerical examples to

demonstrate the capability of the proposed SPH framework for capturing granular material behavior across different phases and geometric conditions. Finally, in the last section, the author has collected together the concluding remarks.

2.1 Physical Laws of Conservation

As granular materials exhibit solid-like behavior, fluid-like behavior and gas-like behavior, the basic governing equations are a combination of the constitutive law in solid mechanics, the conservation laws in fluid mechanics and the equation of state for gas dynamics. Following the standard notation for continuum mechanics [3], the momentum equation is given by

$$\frac{D\mathbf{v}}{Dt} = \frac{1}{\rho}(\nabla \cdot \boldsymbol{\sigma}) + \mathbf{b} \tag{2.1}$$

where $\mathbf{v}$ is the velocity vector, ρ is the material density, $\mathbf{b}$ is the specific body force, and σ is the stress tensor. The total material time derivative is defined as

$$\frac{D()}{Dt} = \frac{\partial()}{\partial t} + \mathbf{v} \cdot \frac{\partial()}{\partial \mathbf{x}} \tag{2.2}$$

and the spatial velocity gradient has the form

$$\mathbf{L} = \nabla \mathbf{v} \tag{2.3}$$

The spin rate tensor and strain rate tensor are defined as

11

$$\mathbf{W} \quad = \quad \frac{1}{2}(\mathbf{L} - \mathbf{L}^T) \tag{2.4}$$

$$\mathbf{D} \quad = \quad \frac{1}{2}(\mathbf{L} + \mathbf{L}^T) \tag{2.5}$$

Writing the trace of the tensor $\mathbf{L}$ as $tr\mathbf{L}$, the conservation of mass is described by

$$\frac{D\rho}{Dt} \quad = \quad -\rho tr\mathbf{L} \tag{2.6}$$

2.2   Constitutive Model

2.2.1   A hyperplastic point of view

In plasticity theory, hyper-plasticity means the strain rate can be decomposed into an elastic and plastic part. Generally, both the elastic and a plastic parts are related to the stress rate via yield or plastic potential functions. To formulate the hyper-plastic constitutive framework, the author starts by the definition of stain rate tensor

$$\mathbf{D} \quad = \quad \mathbf{D}^e + \mathbf{D}^p \tag{2.7}$$

From generalized Hooke's law, the elastic strain rate $\mathbf{D^e}$ tensor is given by,

$$\mathbf{D^e} \quad = \quad \frac{\dot{\mathbf{s}}}{2G} + \frac{1-2\nu}{3E}tr(\dot{\sigma})\delta_{ij} \tag{2.8}$$

where $\dot{\mathbf{s}}$ is the deviatoric shear stress rate tensor, $\dot{\sigma}$ is the Cauchy stress rate tensor, δ_{ij} is the Dirac delta function, ν is the Poisson ratio, E is the Youngs modulus, G and K are the shear modulus and elastic bulk modulus defined as the following,

$$K = \frac{E}{3(1-2\nu)} \quad and \quad G = \frac{E}{2(1+\nu)} \tag{2.9}$$

The plastic strain rate tensor $\mathbf{D^p}$ is given based on the plastic flow rule as,

$$\mathbf{D^p} \quad = \quad \dot{\lambda}\frac{\partial g}{\partial \sigma} \tag{2.10}$$

Here, λ is the plastic multiplier and depends on the stress state and loading history, g is the plastic potential function, specifying the direction of development of plastic strain. It the plastic potential function is related with the yield function f, the flow rule is associated; otherwise, it is non-associated. The plastic multiplier λ can be computed by using the consistency condition, which is

$$df \quad = \quad \frac{\partial f}{\partial \sigma}d\sigma \tag{2.11}$$

Thus the total strain rate tensor is given as follows,

$$\mathbf{D} \ = \ \frac{\dot{\mathbf{s}}}{2G} + \frac{1-2\nu}{3E}tr(\dot{\sigma})\delta_{ij} + \dot{\lambda}\frac{\partial g}{\partial \sigma} \tag{2.12}$$

The total stress tensor is defined as

$$\sigma \ = \ \mathbf{s} + \frac{1}{3}tr\sigma\delta_{ij} \tag{2.13}$$

After using the above two equations, the generalized constitutive relationship for hyperplastic material is derived as follows,

$$\dot{\sigma} \ = \ 2G\dot{\mathbf{e}} - Ktr(\mathbf{D})\delta_{ij} - \dot{\lambda}[(K - \frac{2}{3}G)tr(\frac{\partial g}{\partial \sigma})\delta_{ij} + 2G\frac{\partial g}{\partial \sigma}] \tag{2.14}$$

where $\dot{e}$ is the deviatoric strain rate tensor defined as,

$$\dot{\mathbf{e}} \ = \ \mathbf{D} - \frac{1}{3}tr(\mathbf{D})\delta_{ij} \tag{2.15}$$

By substituting Eq. (2.8) into consistency condition, the rate of change of plastic multiplier can be obtained through

$$\dot{\lambda} \ = \ \frac{2G\mathbf{D} : \dfrac{\partial f}{\partial \sigma} + (K - \dfrac{2G}{3})tr(\mathbf{D})\dfrac{\partial f}{\partial \sigma} : \delta_{ij}}{2G\dfrac{\partial f}{\partial \sigma} : \dfrac{\partial g}{\partial \sigma} + (K - \dfrac{2G}{3})\dfrac{\partial f}{\partial \sigma} : \delta_{ij}\dfrac{\partial g}{\partial \sigma} : \delta_{mn}} \tag{2.16}$$

For the Drucker-Prager material with associated failure flow rule, the yield potential function $f(\sigma)$ and plastic potential function $g(\sigma)$ are given by,

$$f(I_1, \sqrt{J_2}) \quad = \quad \sqrt{J_2} + \alpha_\phi I_1 - k_c \tag{2.17}$$

$$g(I_1, \sqrt{J_2}) \quad = \quad \sqrt{J_2} + \alpha_\phi I_1 - k_c \tag{2.18}$$

For non-associated flow rule, the plastic potential function has the following

form:

$$g(I_1, \sqrt{J_2}) \quad = \quad \sqrt{J_2} + 3I_1 sin(\psi) \tag{2.19}$$

where I_1 and J_2 are the first and second invariants of the stress tensor, given

by

$$I_1 = tr(\sigma) \quad and \quad J_2 \quad = \quad \frac{1}{2}\mathbf{s} : \mathbf{s} \tag{2.20}$$

α_ϕ and k_c are Drucker-Prager's constants related to the Coulomb's constants

c (cohesion) and ϕ (friction angle). For the plain strain assumption, the Drucker-

Prager's constants become,

$$\alpha_\phi \quad = \quad \frac{\tan \phi}{\sqrt{9 + 12 \tan^2 \phi}} \quad and \quad k_c = \frac{3c}{\sqrt{9 + 12 tan^2(\phi)}} \tag{2.21}$$

After substituting the plastic and yield potential functions into the definition

of stress rate tensor and the rate of change of plastic multiplier, the hyperplastic

constitutive law with associated flow rule is as follows:

$$\dot{\sigma} = 2G\dot{\mathbf{e}} - K tr(\mathbf{D})\delta_{ij} - \dot{\lambda}(3K\alpha_\phi\delta_{ij} + \frac{G}{\sqrt{J_2}}\mathbf{s}) \qquad (2.22)$$

The corresponding rate of change of plastic multiplier is

$$\dot{\lambda} = \frac{3\alpha_\phi K tr(\mathbf{D}) + \frac{G}{\sqrt{J_2}}\mathbf{s} : \mathbf{D}}{9\alpha_\phi^2 K + G} \qquad (2.23)$$

The hyperplastic constitutive law with non-associated flow rule is as follows:

$$\dot{\sigma} = 2G\dot{\mathbf{e}} - K tr(\mathbf{D})\delta_{ij} - \dot{\lambda}(9K sin(\psi)\delta_{ij} + \frac{G}{\sqrt{J_2}}\mathbf{s}) \qquad (2.24)$$

The corresponding rate of change of plastic multiplier is

$$\dot{\lambda} = \frac{3\alpha_\phi K tr(\mathbf{D}) + \frac{G}{\sqrt{J_2}}\mathbf{s} : \mathbf{D}}{27\alpha_\phi K sin(\psi) + G} \qquad (2.25)$$

Taking into the material frame-indifference into account, the Jaumann stress rate is

$$\dot{\hat{\sigma}} = \dot{\sigma} + \sigma\dot{\omega} - \omega\dot{\sigma} \qquad (2.26)$$

where $\dot{\omega}$ is the spin rate tensor. Thus the final form of hyperplastic constitutive relationship with associated flow rule is,

$$\dot{\sigma} + \sigma\dot{\omega} - \omega\dot{\sigma} \quad = \quad 2G\dot{\mathbf{e}} - Ktr(\mathbf{D})\delta_{ij} - \dot{\lambda}(3K\alpha_\phi\delta_{ij} + \frac{G}{\sqrt{J_2}}\mathbf{s}) \qquad (2.27)$$

Thus, the final form of hyperplastic constitutive relationship with non-associated flow rule is obtained as

$$\dot{\sigma} + \sigma\dot{\omega} - \omega\dot{\sigma} \quad = \quad 2G\dot{\mathbf{e}} - Ktr(\mathbf{D})\delta_{ij} - \dot{\lambda}(9Ksin(\psi)\delta_{ij} + \frac{G}{\sqrt{J_2}}\mathbf{s}) \qquad (2.28)$$

2.2.2 A viscoplastic point of view

A viscoplastic constitutive relationship developed for granular material in dense regime is adopted and revised from earlier work [19] to describe the granular media by the following equation:

$$\boldsymbol{\sigma} \quad = \quad \begin{cases} -P\mathbf{I} + \dfrac{(\mu P + c)\mathbf{D}}{|\mathbf{D}|} & \text{for} \quad I \geq 0.001 \\[4mm] -P\mathbf{I} + (\mu P + c)sign(\mathbf{D}) & \text{for} \quad I < 0.001 \end{cases} \qquad (2.29)$$

Here, the first term in Eq. (2.29) is the hydro-static pressure, and the second term in Eq. (2.29) is the deviatoric shear stress, μ is the friction coefficient, P is the pressure, c is representative of cohesion, $\mathbf{I}$ is the identity tensor, I is the inertial number (when I <0.001, the granular material is in quasi-static regime and when I $\geq$0.001 the granular material is in dense regime from [12]) and $|\mathbf{D}| = \sqrt{\frac{1}{2}\mathbf{D} : \mathbf{D}}$ is the second invariant of the strain rate tensor. To avoid singularities, $|\mathbf{D}| + \epsilon$ is

adopted and ϵ is set to $0.01h^2$ in the numerical simulation as suggested in previous work [27]. The pressure is determined by using the equation of state as follows,

$$
P \;=\; \begin{cases} \kappa[(\dfrac{\rho}{\rho_o})^\gamma - 1](1+w) & \text{for} \quad \rho > \rho_o \\[4mm] 0 & \text{for} \quad \rho \le \rho_o \end{cases} \tag{2.30}
$$

wherein ρ_o is the reference density, κ is related to the bulk modulus and set to 28000, w is the gravimetric water content (the ratio between the weight of water and the weight of the dry granular particles), γ is a scaling parameter and set to 7 as suggested in the literature [33]. The friction law follows from reference [19], [20] and reads as

$$
\mu(I) \;=\; \mu_1 + \frac{\mu_2 - \mu_1}{I_o/I + 1} \tag{2.31}
$$

Here, μ_1 is the friction coefficient for the quasi-static limit, μ_2 is a limiting coefficient for granular material in the dynamic flow regime, and I is the inertia number defined as,

$$
I \;=\; \frac{|\mathbf{D}|d}{\sqrt{P/\rho_s}} \tag{2.32}
$$

In Eq.(2.32), d is the grain diameter and set to 0.002m for all of the simulations and ρ_s is the particle density. For dry cohesionless particles, c is set to 0. For wet granular particles in the pendular state, the cohesion arises from surface tension and capillary strengthening effects. Rumpf [43] estimated cohesive stress for isotropic

18
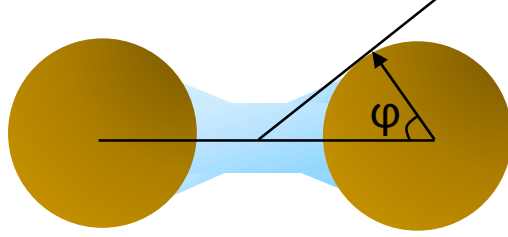
Figure 2.1:   Illustration of liquid bridge between two granular material particles.

granular material with identical diameters as

$$c \quad = \quad \frac{\nu k F}{\pi d^2} \tag{2.33}$$

where ν is the grain packing fraction. For all the wet granular material simulations in this chapter, k is assumed to be 6 accrording to experimental results from [15] and [16], which is the average number for the liquid bridge between a pair of particles, and F is the average force per liquid bridge that is given by

$$F \quad = \quad \frac{2\pi r \gamma_s}{1 + \tan(\varphi/2)} \tag{2.34}$$

where r is the grain radius, γ_s is the surface tension, and φ is defined in Fig. 2.1. Note that the particles in Fig. 2.1 are not SPH partilces but real granular material particles. In the simulation, parameters are taken from physical experiments [45].
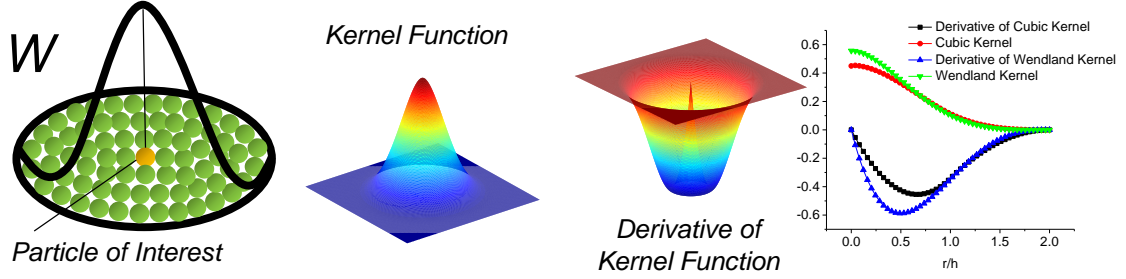
Figure 2.2: Kernel function.

2.3 Numerical Implementation

2.3.1 The SPH method

Smoothed particle hydrodynamics is a mesh-free Lagrangian method. As with other discretization approaches, in the SPH method, the solution domain is first discretized and represented by a certain number of particles [35], [36]. Thus, all the field properties, such as density, velocity, and strain rate, are carried by these SPH particles. The properties of the particles of interest are then interpolated over their neighboring particles by using an approximation function, called the kernel function, which is usually represented by W (see Fig. 2.2). The most popular cubic kernel function from reference [35], takes the following form:

$$W_{ij} = \alpha_d \times \begin{cases} \dfrac{2}{3} - q^2 + \dfrac{1}{2}q^3 & \text{for} \quad 0 \leq q < 1 \\[2mm] \dfrac{1}{6}(2-q)^3 & \text{for} \quad 1 \leq q < 2 \\[2mm] 0 & \text{for} \quad 2 \leq q \end{cases} \tag{2.35}$$

Here, for one-dimensional, two-dimensional, and three-dimensional problems,

α_d is set to $1/h$, $15/(7\pi h^2)$, and $3/(2\pi h^2)$, respectively, $q = r/h$, r is the distance between two particles, and h is the smoothing length. Although the above most popular B-spline kernel function often yields a good balance between accuracy and stability, the Wendland kernel function is adopted from [46] in this work to provide robust and stable solutions without using artificial stress method [44]. This function takes the following form:

$$
W_{ij} = \alpha_d \times
\begin{cases}
(1 - \frac{q}{2})^4(2q + 1) & \text{for} \quad q \leq 2 \\
\\
0 & \text{otherwise}
\end{cases}
\tag{2.36}
$$

Here, for two-dimensional and three-dimensional problems, α_d is set to $7/(4\pi h^2)$ and $21/(16\pi h^3)$, respectively, $q = r/h$, r is the distance between two particles, and h is the smoothing length. Then, the particle approximation/interpolation for any field quantity $f(x)$ and its derivatives at point i can be expressed as

$$
f(\mathbf{x_i}) = \sum_{j=1}^{N} \frac{m_j}{\rho_j} f(\mathbf{x_j}) W_{ij}
\tag{2.37}
$$

$$
\nabla f(\mathbf{x_i}) = \sum_{j=1}^{N} \frac{m_j}{\rho_j} f(\mathbf{x_j}) \nabla_{\mathbf{i}} \mathbf{W_{ij}}
\tag{2.38}
$$

where $W_{ij} = W(\mathbf{r_{ij}}, h)$ and

$$
\nabla_i W_{ij} = \frac{\mathbf{x_i} - \mathbf{x_j}}{r_{ij}} \frac{\partial W_{ij}}{\partial r_{ij}}
\tag{2.39}
$$

2.3.2 SPH for granular flow

Summation density: Two approaches to evolve density are adopted in the SPH framework. For density initialization of a particle i, the density calculated by using the summation density approach is written as

$$\rho_i \;=\; \sum_j m_j W_{ij} \tag{2.40}$$

For density re-initialization, the Shepard filter is applied every 10 time steps to reduce the inaccuracies near the boundaries and free surfaces; this is given by

$$\rho_i \;=\; \frac{\displaystyle\sum_j m_j W_{ij}}{\displaystyle\sum_j \frac{m_j}{\rho_j} W_{ij}} \tag{2.41}$$

Continuity density: For density evolution at each time step, the continuity density is calculated from the continuity equation. The δ SPH scheme is adopted from reference [42] to reduce high-frequency oscillations by introducing a diffusive term that takes the form

$$\frac{D\rho_i}{Dt} \;=\; \sum_j m_j(\mathbf{v_i} - \mathbf{v_j}) \cdot \nabla_i \mathbf{W_{ij}} + \sum_j \psi_{ij}\mathbf{r_{ij}}\nabla_i \mathbf{W_{ij}} \tag{2.42}$$

where ψ_{ij} is defined as

$$\psi_{ij} \;=\; \frac{2\delta h c_o(\rho_j - \rho_i)m_j}{\rho_j |\mathbf{r_{ij}}^2|} \tag{2.43}$$

Here, δ is set to 0.01, c_o is the artificial sound speed set as

$$c_o = \sqrt{\frac{\kappa\gamma\rho_s}{\rho_o(\rho_s - \rho_o)}} \tag{2.44}$$

Particle approximation of momentum: To reduce errors associated with particle inconsistencies, the momentum equation is approximated as

$$\frac{D\mathbf{v_i}}{Dt} = \sum_j m_j \left(\frac{\boldsymbol{\sigma}_i}{\rho_i^2} + \frac{\boldsymbol{\sigma}_j}{\rho_j^2} - \Pi_{ij}\right) \cdot \nabla_i \mathbf{W_{ij}} + \mathbf{b} \tag{2.45}$$

where $\mathbf{b}$ is the body force. The quantity Π is the artificial viscosity adopted to improve numerical stability and avoid inter-particle penetration. This quantity is formulated as

$$\Pi_{ij} = \begin{cases} \dfrac{-\alpha_\Pi c_{ij}\phi_{ij} + \beta_\Pi \phi_{ij}^2}{\rho_{ij}} & \text{for} \quad v_{ij} \cdot x_{ij} < 0 \\ \\ 0 & \text{for} \quad 0 \leq v_{ij} \cdot x_{ij} \end{cases} \tag{2.46}$$

$$\phi_{ij} = \frac{h_{ij}\mathbf{v_{ij}} \cdot \mathbf{x_{ij}}}{|\mathbf{x_{ij}}|^2 + 0.01h_{ij}^2} \tag{2.47}$$

Here, $c_{ij} = (c_i + c_j)/2$, here both c_i and c_j are set to c_o as defined in Eq.(2.44), $\rho_{ij} = (\rho_i + \rho_j)/2$, $h_{ij} = (h_i + h_j)/2$, and $\mathbf{x_{ij}} = \mathbf{x_i} - \mathbf{x_j}$, $\mathbf{v_{ij}} = \mathbf{v_i} - \mathbf{v_j}$. c is computed through Eq.(2.44), α_Π is set to 1 and β_Π is set to 0 as the second quadratic term in the artificial viscosity is used to handle high Mach number flows [47].To evaluate the

stress tensor in Eq.(2.45), the velocity gradient needs to be interpolated as follows

$$\nabla \mathbf{v_i} \;\; = \;\; \sum_j \frac{m_j}{\rho_j} (\mathbf{v_j} - \mathbf{v_i}) \otimes \nabla_i \mathbf{W_{ij}} \tag{2.48}$$

The extended Smoothed Particle Hydrodynamics (XSPH) is employed from prior work [35] to stabilize particles at free surfaces and avoid unphysical penetration. This is given by

$$\frac{d\mathbf{r_i}}{dt} \;\; = \;\; \mathbf{v_i} + \chi \sum_j \frac{m_j}{\rho_{ij}} (\mathbf{v_j} - \mathbf{v_i}) W_{ij} \tag{2.49}$$

where χ is set to 0.2.

2.3.3   Boundary conditions

Two types of boundary conditions are employed in this research. The first is the solid boundary wall. To generate a solid boundary, the stress tensor for solid boundary particles is calculated by using Eq. (2.29). Also, ghost particles are used to remove the boundary inaccuracies in SPH methods. The velocity and stress for the ghost particles are set in accordance with earlier work [28].

2.3.4   Integration

For integrating the Newton's law of motion, the popular Verlet-Leapfrog algorithm is used. In adopting this approach, the field variables such as density, velocity vectors, and position vectors are updated at every time step as follows,

$$\rho_i^{n+1/2} \quad = \quad \rho_i^{n-1/2} + \Delta t \frac{D\rho_i}{Dt}^n \tag{2.50}$$

$$\mathbf{v}_i^{n+1/2} \quad = \quad \mathbf{v}_i^n + \frac{\Delta t}{2} \frac{D\mathbf{v}_i}{Dt}^n \tag{2.51}$$

$$\mathbf{r}_i^{n+1/2} \quad = \quad \mathbf{r}_i^n + \frac{\Delta t}{2} \mathbf{v}_i^{n+1/2} \tag{2.52}$$

The Courant-Friedrichs-Lewy condition is used to determine the time step to satisfy the following,

$$\Delta t \quad \leq \quad C_{cour}(\frac{h}{c_s}) \tag{2.53}$$

Here, h is the smoothing length, c_s is the sound speed calculated by Eq.(2.44), and C_{cour} is the Courant coefficient.

2.4   Results and Discussion

The granular column collapse case is employed to test the rheology based constitutive relationship used for wet granular materials. It is shown that the results generated from the current constitutive law are consistent with experimental findings for both dry and wet cases, as illustrated in Fig. 2.3. The parameters μ_1 and μ_2 correspond approximately to parameters of glass beads in [19] are used in the implementation of the friction law for both the dry granular media and wet granular media studies. (The full list of parameters are shown in Table 2.1 consistent
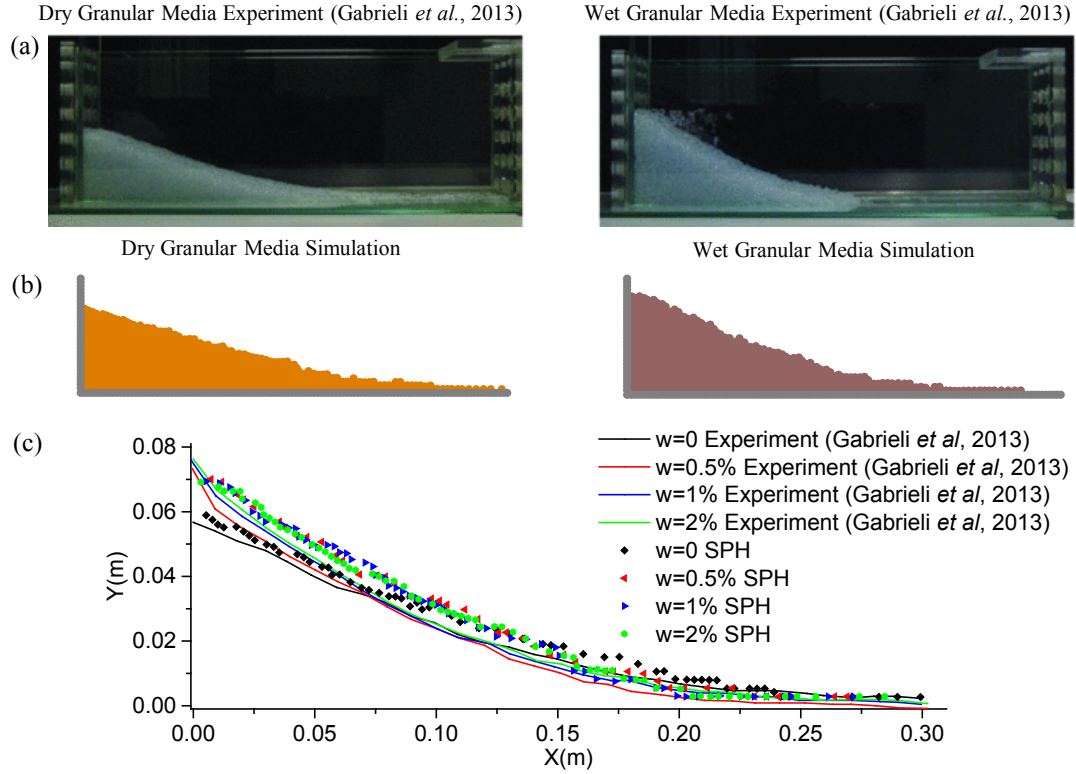
Figure 2.3: Validation of final profiles for d=2mm. (**a**) Experimental results from literature [45]. (**b**) Computational results obtained in the current work for dry and wet conditions: dry granular media simulation (μ_1=tan(21°), μ_2=tan(33°), w=0) and wet granular media simulation (μ_1=tan(21°), μ_2=tan(33°), w=0.5%). (**c**) Simulated and experimental final profiles for different water content.

with [23]). In Fig. 2.3a, two typical final configurations of wet and dry granular column collapse are shown from [23]. In Fig. 2.3b, the qualitative results of two typical simulations of wet and dry granular column collapses are shown, which is similar to the experimental findings in [23]. It is evident that larger cohesion in wet granular column collapses gives rise to a shorter run-out length and larger angles of repose. In Fig. 2.3c, k is assumed to be 6 for all the wet granular material simulations, accrording to experimental results from [15] and [16]. The grain diameter d is 0.002m. The final profiles are shown with the increase of liquid content. In the simulations, the results of the influence of liquid content on the final profiles are similar to experimental findings. Dry and wet conditions seem distinct, while differences between wet cases seem smaller. Having verified that the proposed SPH formulation can be used for dry granular media and wet granular media studies, the authors then consider other illustrative cases.

Next, the authors consider transient and steady-state phenomena and associated characteristics related to particle dynamics during granular column collapses, such as runout distance, the angle of repose, strain developed during the collapse. The shear strength properties are also studied to uncover clues related to the underlying mechanisms during the collapse.

2.4.1   Runout dynamics of granular column collapse on flat surfaces

The geometry of the quasi-2D initial configuration (7x8 cm^2) and surface profile of the final configuration of the granular column is shown in Fig. 2.4. The
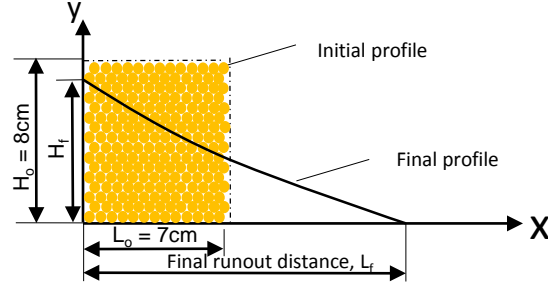
Figure 2.4: Initial geometry and final geometry of granular column.

particles are aligned in a particular arrangement layer by layer. For all of the numerical results shown for dry and wet granular materials studied in this chapter, the parameter values are set to be the same as what is shown in Fig. 2.3.

Table 2.1: Parameters used in simulations of the dry granular column and wet granular column collapse

Simulation	$\rho_s(kg/m^3)$	$\rho_o(kg/m^3)$	k	$\Delta x(m)$	$\gamma_s(mN/m)$	$d(m)$	φ
Dry	2532	2507	0	0.0026	0	0.002	0
Wet	$2532*(1+w)$	$2507*(1+w)$	6	0.0026	72.5	0.002	15°

The influence of wetting fluid on the run-out dynamics of wet and dry granular column collapse is shown in Fig. 2.5. It is evident that a small amount of fluid between granular particles impacts the deposit as well as the final shape of the run-out dynamics. In Fig. 2.5a, the representative profiles of low friction, dry and wet granular materials at different time instants are presented. At t= 0.01s, the collapse is triggered and the material starts to flow under gravity; At t= 0.2s, the collapse is well developed, the material near the boundary is in the quasi-static
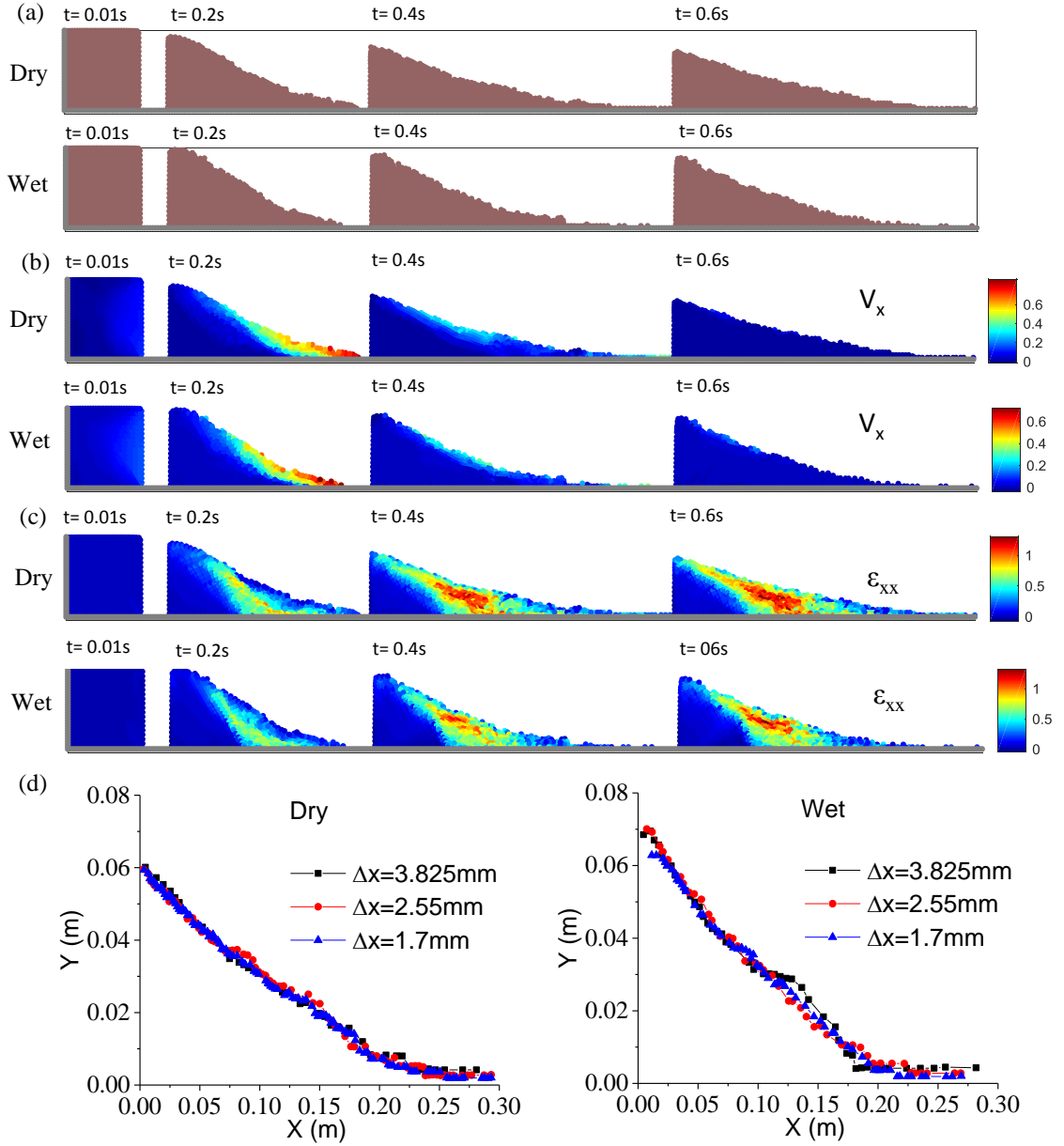
Figure 2.5: Run-out dynamics during the collapse of dry granular material ($\mu_1=\tan(21^o)$, $\mu_2=\tan(33^o)$, w=0) and wet granular material ($\mu_1=\tan(21^o)$, $\mu_2=\tan(33^o)$, w=0.5%). (**a**) Profiles of dry and wet granular materials at different time instants. (**b**) Velocity profiles of dry and wet granular materials at different time instants. (**c**) Strain developed during the collapse of dry and wet granular columns at different time instants. (**d**) Final profiles with different resolution.

regime and the material near the surface is in the dynamic flow regime. At t = 0.4s, the occurrence of jamming due to friction at the boundary prevents further collapse. By t = 0.6s, one can infer that the internal stresses are quite well distributed and appear to be in a quasi-steady state, particularly in regions close to the boundary and the surface. It is observed that the wet granular material has a shorter run-out distance compared to dry granular material. In Fig. 2.5b, the horizontal velocity contours are presented for dry and wet granular material at different time instants. It is clear that the wet granular column collapses more slowly than in the dry case because of the surface tension induced cohesive stress. In Fig. 2.5c, the strain developed during the collapse is shown. The wet granular material is noted to deform less than the dry granular material at all representative time instants due to the presence of cohesion. The low level of deformation of wet granular materials leads to a shorter run-out distance and higher final height. In Fig. 2.5d, final profiles of dry and wet granular columns for different resolutions are shown. The number of interior SPH particles are 475, 1036, and 2310 accordingly for the coarsest resolution, the fit resolution and the finest resolution. The fit resolution is used in other simulations in this chapter, since both the results generated using the finest and fit resolution agree with the experimental findings from [45]. In Fig. 2.6a, steady state profiles of granular materials are shown for different water content and friction levels (μ_1=tan(21°), μ_2=tan(33°); μ_1=tan(32°), μ_2=tan(33°); μ_1=tan(32°), μ_2=tan(45°)). For low frictional granular materials, dry and wet conditions seem distinct, while differences between wet cases of different water content seem smaller. For high frictional granular materials, differences between wet and dry cases are
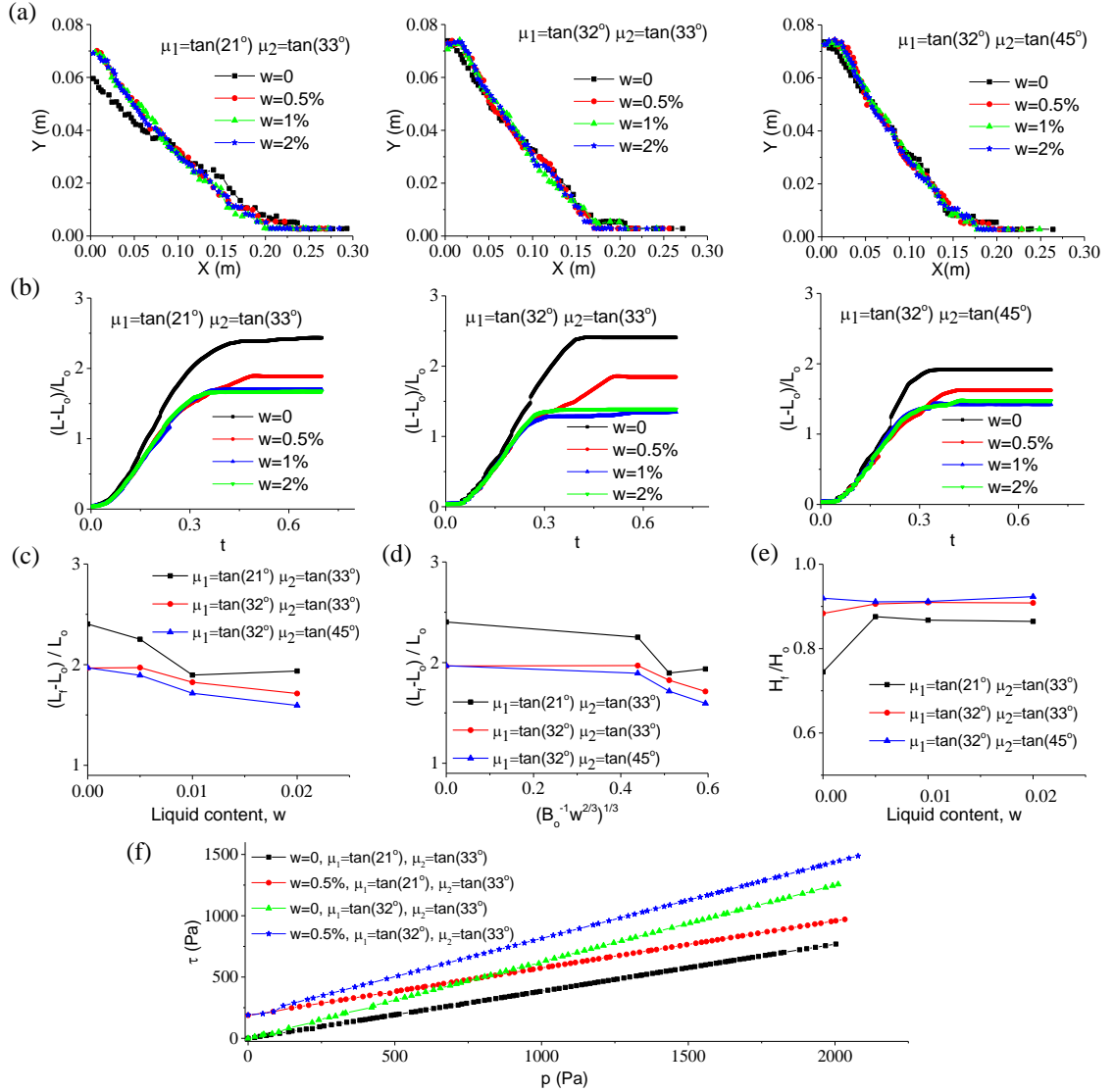
Figure 2.6: Parametric study of dry and wet granular column collapses on flat surfaces. (**a**) Final profiles of granular materials for different friction levels and water contents. (**b**) Normalized run-out length during granular column collapses for different friction levels and water contents. (**c**) Normalized final run-out length for different friction levels and water contents. (**d**) Normalized final run-out length vs dimensionless number $Bo^{-1}w^{2/3}$ for different water content. (**e**) Normalized final height for different friction levels and water contents. (**f**) Yield loci τ-σ of dry and wet granular materials in the final state.

31

small. In the pendular state, the final profile of the wet granular materials depends on both the water content and friction levels. The differences in water content play a more prominent role in low friction granular materials compared with high friction granular materials. In Fig. 2.6b, front advancement (normalized run-out distance) during granular column collapses at different time instants is displayed. It is shown that the granular materials reach steady state before 0.6s. The run-out distance is rescaled and non-dimensionalized by $L^* = (L - L_o)/L_o$, where L_o is the initial length of the granular column, and L is the run-out distance of each state. In Fig. 2.6c, the final normalized run-out distance is plotted for different friction and water content levels. L_f is the run-out distance of the final state. The increase of water content has a strong influence on the final runout distance when the water content is less than 1%, and small effect when the water content is larger than 1%. In Fig. 2.6d, the normalized run-out distance is plotted with respect to a dimensionless number as a function of Bond number $Bo = \rho g R^2/\gamma$, which is the ratio between the body force and capillary force, and the water content ω. In Fig. 2.6e, the final normalized height is plotted for different friction levels and water contents. H_f is the height of the final state. The final height is rescaled and non-dimensionalized by $H^* = H_f/H_o$, where H_o is the initial height of the granular column. In Fig. 2.6f, the authors plot the absolute value of the maximum shear stress in the material along the pressure isobar for different friction levels of dry and wet granular materials. The yield τ-p loci are plotted and the relationship is close to a straight line, which is in agreement with the Drucker-Prager model as the granular material is in quasi-static regime. It is shown that, in the pendular state, the introduction of capillary force

increases the shear strength which in turn enables a stronger granular structure.

2.4.2   Gravity driven granular flow on curved surfaces

Although the primary driving force for a landslide or landslide-like phenomenon is gravity, other contributing factors affect the slope stability. To simulate granular flows across nature-like surfaces and benchmark the author's numerical model for wet granular material, wet granular flows across different topology and geometry conditions are presented, ranging from circular surfaces to ellipsoidal surfaces. The influence of wetting fluid on the run-out dynamics of wet and dry granular column collapses on curved surfaces is shown in Fig. 2.7 and Fig. 2.8. For collapses of granular columns on curved surfaces, what is similar to collapses of granular column on flat surfaces is that: in Fig. 2.7a and Fig. 2.8a, the representative profiles of low friction, dry and wet granular materials at different time instants are presented. Wet granular materials deform less than dry granular materials at all time instants during the collapses. In Fig. 2.7b and Fig. 2.8b, the velocity contours are presented for dry and wet granular materials at different time instants. Wet granular column collapses more slowly than dry granular columns because of the surface tension induced cohesion. In Fig. 2.7c and Fig. 2.8c, steady state granular profiles are shown for different levels of water content and friction. In Fig. 2.7d and Fig. 2.8d, the yield τ-p loci for dry and wet granular materials are plotted and the relationship is close to a straight line, which is in agreement with the Drucker-Prager model as the granular material is in quasi-static regime. It is shown that, in the pendu-
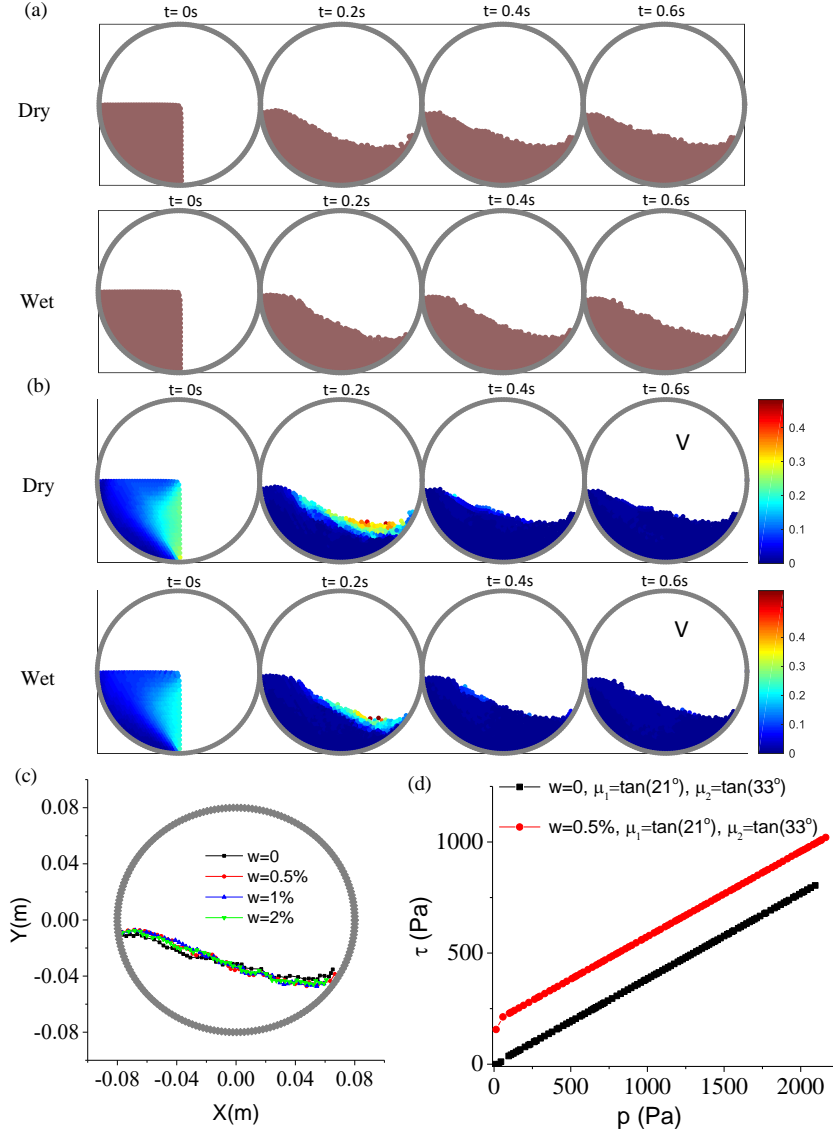
Figure 2.7: Granular flows on circular surfaces for d=0.002m. (**a**) Profiles of dry granular material (μ_1=tan(21°), μ_2=tan(33°), w=0) and wet granular material (μ_1=tan(21°), μ_2=tan(33°), w=0.5%) on circular surfaces at different time instants. (**b**) Velocity profiles of dry granular material and wet granular material on circular surfaces at different time instants. (**c**) Final profiles of granular material on circular surfaces for different water contents. (**d**) Yield loci τ-σ of granular flows on circular surfaces in the final state.
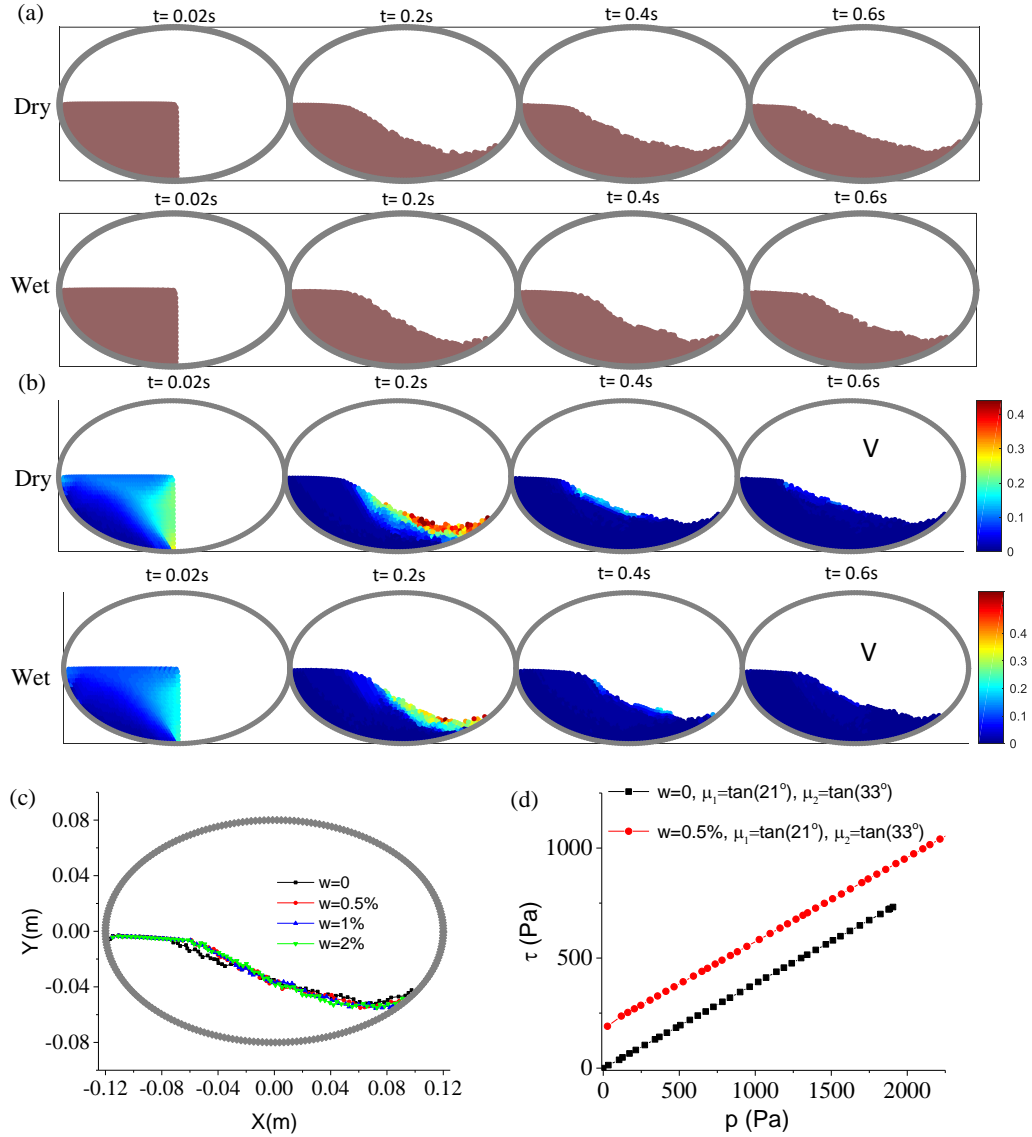
Figure 2.8: Granular flows on ellipsoidal surfaces for d=0.002m. (**a**) Profiles of dry granular material (μ_1=tan(21°), μ_2=tan(33°), w=0) and wet granular material (μ_1=tan(21°), μ_2=tan(33°), w=0.5%) on ellipsoidal surfaces at different time instants. (**b**) Velocity profiles of dry granular material and wet granular material on ellipsoidal surfaces at different time instants. (**c**) Final profiles of granular material on ellipsoidal surfaces for different water contents. (**d**) Yield loci τ-σ of granular flows on ellipsoidal surfaces in the final state.

lar state, the introduction of capillary force increases the shear strength that make the entire granular structure deform less. However, for granular column collapses on curved surfaces, although the introduction of capillary force increases the shear strength, the differences in final profiles between wet granular materials and dry granular materials are not as pronounced as that on flat surfaces due to geometric constraints. The geometric constraints of circular and ellipsoidal surfaces hinder the further deformation of granular columns. For collapses on ellipses surfaces, dry and wet conditions seemed more distinct than those on circular surfaces. This indicates the smaller the curvature of the surface is, the more distinct the differences between dry and wet conditions will be.

2.5 Concluding Remarks

A constitutive model for both the dry and wet granular materials is implemented in a smoothed particle hydrodynamics framework to investigate the collapse of granular columns on flat and curved surfaces. The grain-scale capillary interaction is taken into consideration for capturing the behavior of wet granular materials. The proposed SPH framework is validated by comparing numerical results obtained with this model with recent experimental findings for dry and wet granular column collapses on flat surfaces. Compared with dry granular materials, the introduction of surface tension in wet granular materials is noted to increase the shear stresses and enable a stronger structure with larger angles of repose. Although experimental validation was not found for the simulations of collapses on curved surfaces, future

experimental studies may find the results useful to compare with. For collapses on curved surfaces, the differences in final profiles between wet granular materials and dry granular materials are not as pronounced as that on flat surfaces due to geometric constraints, although there is also an increase in internal shear strength. Through the current study, it is shown that the smoothed particle hydrodynamics method can be used to study wet granular materials.

Chapter 3:   Single Robot Appendage Interaction with Soft Terrain

Legged locomotion has advantages when one is navigating a flowable ground
or a terrain with obstacles that are common in nature. With traditional terra-
mechanics, one can capture large wheel-terrain interactions. However, legged motion
on a granular substrate is difficult to investigate by using classical terra-mechanics
due to sharp-edge contact. Recent studies have shown that a continuum simulation
can serve as an accurate tool for simulating dynamic interactions with granular ma-
terial at laboratory and field scales. No studies have been conducted on continuum
modeling of interactions between flowable terrain and robot limbs and appendages
across different leg morphology as shown in Fig. 1.2. This is addressed here. Spurred
by this, a computational framework based on the Smoothed particle hydrodynamics
(SPH) method has been developed for the investigation of single robot appendage
interaction with a granular system. This framework has been validated by using
experimental results and extended to study robot appendages with different shapes
and stride frequencies. The results are expected to help robot navigation and ex-
ploration in unknown and complex terrains. The rest of this chapter [1] is organized

---

[1] Disclosure: This chapter has been adapted from the accepted work, Wang, G., Riaz, A. and
Balachandran, B., 2020. Continuum Modeling and Simulation of Robotic Appendage Interaction
with Granular Material. ASME Journal of Applied Mechanics, in press

into four sections to include the formulation, numerical implementation, results, and concluding remarks.

3.1 Governing Equations

The underlying mechanics is based on the author's previous work [58]. In this section, the adaption of this work to study the current problems of interest is described.

3.1.1 Physical laws of conservation

Following the standard notation for continuum mechanics, the momentum equation is given by

$$\frac{D\mathbf{v}}{Dt} = \frac{1}{\rho}(\nabla \cdot \boldsymbol{\sigma}) + \mathbf{b} \tag{3.1}$$

where $\mathbf{v}$ is the velocity vector, ρ is the material density, $\mathbf{b}$ is the specific body force, and σ is the Cauchy stress tensor. The total material time derivative is defined as

$$\frac{D()}{Dt} = \frac{\partial()}{\partial t} + \mathbf{v} \cdot \frac{\partial()}{\partial \mathbf{x}} \tag{3.2}$$

The conservation of mass is described by

$$\frac{D\rho}{Dt} = -\rho tr\mathbf{L} \tag{3.3}$$

where $\mathbf{L}$ is the spatial velocity gradient has the form $\mathbf{L} = \nabla \mathbf{v}$ and its trace is $tr\mathbf{L}$.

Here, the robot limb or appendage is treated as a rigid body composed of particles. The interactive forces and torque between the granular material and robot leg are determined as follows:

$$\mathbf{F}_{granular-robot} = \int_{\Gamma} \mathbf{n} \cdot \boldsymbol{\sigma} d\mathbf{x} \tag{3.4}$$

$$\mathbf{T}_{granular-robot} = \int_{\Gamma} \mathbf{r} \times (\mathbf{n} \cdot \boldsymbol{\sigma}) d\mathbf{x} \tag{3.5}$$

3.1.2 Constitutive law

As things stand, there is no unified constitutive model for granular materials [59]. Some scholars prefer Drucker-Prager model with different flow rules [29], while others like the $\mu(I)$ rheology better [26]. There are no big differences between the two different models for simulating the collapses of the granular columns. The author has chosen the following visco-plastic constitutive relationship because it is simple enough to capture the physics between robot leg interaction and granular material. The first equation is the same as $\mu(I)$ rheology used in prior work [19] . With just the first equation, it has been reported in earlier work [27] and also found in the author's prior work [58], that one has oscillations in the stress field. Therefore, the second equation has been proposed to smooth the fluctuations out in the strain rate

field and also enable the material to sustain shear stress at zero stain rate:

$$\sigma \;=\; \begin{cases} -P\mathbf{I} + \dfrac{(\mu P + c)\mathbf{D}}{|\mathbf{D}|} & \text{for} \quad I > 0.001 \\[4mm] -P\mathbf{I} + \dfrac{(\mu P + c)\mathbf{E}}{|\mathbf{E}|} & \text{for} \quad I \leq 0.001 \end{cases} \tag{3.6}$$

Here, the first term in both equations of Eq. (3.6) is the hydro-static pressure, and the second term in both equations of Eq. (3.6) is the deviatoric shear stress, μ is the friction coefficient, P is the pressure, c is representative of cohesion, $\mathbf{I}$ is the identity tensor, I is the inertial number (when I <0.001, the granular material is in quasi-static regime and when I $\geq$0.001 the granular material is in dense regime from [61]). The strain rate tensor is defined as $\mathbf{D} = \frac{1}{2}(\mathbf{L} + \mathbf{L}^T)$. $|\mathbf{D}| = \sqrt{\frac{1}{2}\mathbf{D} : \mathbf{D}}$ is the second invariant of the strain rate tensor. $|\mathbf{E}| = \sqrt{\frac{1}{2}\mathbf{E} : \mathbf{E}}$ is the second invariant of the strain tensor $\mathbf{E}$, where $\mathbf{E} = \frac{1}{2}(\nabla\mathbf{x} + \nabla\mathbf{x}^T)$. To avoid singularities, $|\mathbf{D}| + \epsilon$ and $|\mathbf{E}| + \epsilon$ are adopted and ϵ is set to $0.01h^2$ in the numerical simulation as suggested in previous work [27]. The pressure is determined by using the equation of state as follows

$$P \;=\; \begin{cases} \kappa[(\dfrac{\rho}{\rho_o})^{\gamma} - 1] & \text{for} \quad \rho > \rho_o \\[4mm] 0 & \text{for} \quad \rho \leq \rho_o \end{cases} \tag{3.7}$$

wherein ρ_o is the reference density, κ is related to the bulk modulus and set to 30000. The value of κ is chosen according to reference [27], where it has been reported that the simulation results were not sensitively dependent on this parameter in a certain range. Then a small value of κ is picked to use a relatively large time step 10^{-5} to

reduce computational cost. γ is a scaling parameter and set to 7 as suggested in the literature [33]. The friction law follows from reference [19] and reads as

$$\mu(I) \;\; = \;\; \mu_1 + \frac{\mu_2 - \mu_1}{I_o/I + 1} \tag{3.8}$$

Here, μ_1 is the friction coefficient in the quasi-static limit, μ_2 is a limiting coefficient for granular material in the dynamic flow regime, and I is the inertia number defined as

$$I \;\; = \;\; \frac{|\mathbf{D}|d}{\sqrt{P/\rho_s}} \tag{3.9}$$

Further, d is the grain diameter and set to 3mm for all of the simulations and ρ_s is the particle density. For dry cohesionless particles, c is set to 0 in Eq. (3.6).

3.2 Numerical Implementation

3.2.1 The SPH method

There are many meshfree methods that share similar discretization features. Smoothed particle hydrodynamics is employed for its simplicity. In the SPH method, the solution domain is first discretized and represented by a certain number of particles [34]. Thus, all of the field properties, such as density, velocity, and strain rate, are carried by these SPH particles. The properties of the particles of interest are then interpolated over their neighboring particles by using the kernel function represented by W. In this work, the Wendland kernel function is adopted from

42

previous work [46] to provide robust and stable solutions. This function takes the following form:

$$W_{ij} \;=\; \alpha_d \times \begin{cases} (1 - \frac{q}{2})^4 (2q + 1) & \text{for} \quad q \leq 2 \\[2em] 0 & \text{otherwise} \end{cases} \tag{3.10}$$

Here, for two-dimensional and three-dimensional problems, α_d is set to $7/(4\pi h^2)$ and $21/(16\pi h^3)$, respectively, $q = r/h$, r is the distance between two particles, and h is the smoothing length. Then, the particle approximation/interpolation for any field quantity $f(x)$ and its derivatives at point i can be expressed as [34]:

$$f(\mathbf{x_i}) = \sum_{j=1}^{N} \frac{m_j}{\rho_j} f(\mathbf{x_j}) W_{ij} \tag{3.11}$$

$$\nabla f(\mathbf{x_i}) = \sum_{j=1}^{N} \frac{m_j}{\rho_j} f(\mathbf{x_j}) \nabla_{\mathbf{i}} \mathbf{W_{ij}} \tag{3.12}$$

Here, $W_{ij} = W(\mathbf{x_{ij}}, h)$ and

$$\nabla_i W_{ij} \;=\; \frac{\mathbf{x_i} - \mathbf{x_j}}{r_{ij}} \frac{\partial W_{ij}}{\partial r_{ij}} \tag{3.13}$$

where $r_{ij} = \sqrt{|\mathbf{x_{ij}}|^2}$.

3.2.2   SPH for granular material

Continuity density: For density evolution at each time step, the continuity density is calculated from the continuity equation. The δ SPH scheme is adopted from

reference [42] to reduce high-frequency oscillations by introducing a diffusive term that takes the form

$$\frac{D\rho_i}{Dt} \;=\; \sum_j m_j(\mathbf{v_i} - \mathbf{v_j}) \cdot \nabla_i \mathbf{W_{ij}} + \sum_j \psi_{ij} \mathbf{x_{ij}} \nabla_i \mathbf{W_{ij}} \tag{3.14}$$

where ψ_{ij} is defined as

$$\psi_{ij} \;=\; \frac{2\delta h c_o(\rho_j - \rho_i)m_j}{\rho_j |\mathbf{x_{ij}}^2|} \tag{3.15}$$

Here, δ is set to 0.01 and c_o is the artificial sound speed set as

$$c_o \;=\; \sqrt{\frac{\kappa \gamma \rho_s}{\rho_o(\rho_s - \rho_o)}} \tag{3.16}$$

Summation density: For density initialization of a particle i, the density calculated by using the summation density approach is written as

$$\rho_i \;=\; \sum_j m_j W_{ij} \tag{3.17}$$

For density re-initialization, the Shepard filter is applied every 100 time steps to reduce the inaccuracies near the boundaries and free surfaces; this is given by

$$\rho_i \;=\; \frac{\sum\limits_j m_j W_{ij}}{\sum\limits_j \dfrac{m_j}{\rho_j} W_{ij}} \tag{3.18}$$

44

Particle approximation of momentum: To reduce errors associated with particle inconsistencies, the momentum equation is approximated as

$$\frac{D\mathbf{v_i}}{Dt} = \sum_j m_j \left(\frac{\boldsymbol{\sigma_i}}{\rho_i^2} + \frac{\boldsymbol{\sigma_j}}{\rho_j^2} - \Pi_{ij} \right) \cdot \nabla_i \mathbf{W_{ij}} + \mathbf{b} \tag{3.19}$$

where $\mathbf{b}$ is the body force. The quantity Π is the artificial viscosity adopted to improve numerical stability and avoid inter-particle penetration. This quantity is formulated as

$$\Pi_{ij} = \begin{cases} \dfrac{-\alpha_\Pi c_{ij} \phi_{ij} + \beta_\Pi \phi_{ij}^2}{\rho_{ij}} & \text{for} \quad \mathbf{v_{ij}} \cdot \mathbf{x_{ij}} < 0 \\ 0 & \text{for} \quad 0 \leq \mathbf{v_{ij}} \cdot \mathbf{x_{ij}} \end{cases} \tag{3.20}$$

$$\phi_{ij} = \frac{h_{ij} \mathbf{v_{ij}} \cdot \mathbf{x_{ij}}}{|\mathbf{x_{ij}}|^2 + 0.01 h_{ij}^2} \tag{3.21}$$

Here, $c_{ij} = (c_i + c_j)/2$, where both c_i and c_j are set to c_o as defined in Eq. (3.16), $\rho_{ij} = (\rho_i + \rho_j)/2$, $h_{ij} = (h_i + h_j)/2$, and $\mathbf{x_{ij}} = \mathbf{x_i} - \mathbf{x_j}$, $\mathbf{v_{ij}} = \mathbf{v_i} - \mathbf{v_j}$. c is computed through Eq.(3.16), α_Π is set to 1 and β_Π is set to 0 as the second quadratic term in the artificial viscosity is used to handle high Mach number flows [47].To evaluate the stress tensor in Eq. (3.19), the velocity gradient needs to be interpolated as follows

$$\nabla \mathbf{v_i} = \sum_j \frac{m_j}{\rho_j} (\mathbf{v_j} - \mathbf{v_i}) \otimes \nabla_i \mathbf{W_{ij}} \tag{3.22}$$

The extended smoothed particle hydrodynamics (XSPH) is employed from

prior work [35] to stabilize particles at free surfaces and avoid unphysical penetration. This is given by

$$\frac{d\mathbf{x_i}}{dt} \;=\; \mathbf{v_i} + \chi \sum_j \frac{m_j}{\rho_{ij}}(\mathbf{v_j} - \mathbf{v_i})W_{ij} \tag{3.23}$$

where χ is set to 0.2. The detailed equation of how to compute the interactive forces and torques are as follows

$$\mathbf{F}_{granular-robot} \;=\; \sum_{k \in robot} \sum_{j \in granular} m_k m_j \left(\frac{\boldsymbol{\sigma_i}}{\rho_i^2} + \frac{\boldsymbol{\sigma_j}}{\rho_j^2} - \Pi_{ij}\right)\nabla_i \mathbf{W_{ij}} \tag{3.24}$$

$$\mathbf{T}_{granular-robot} \;=\; \sum_{k \in robot} \sum_{j \in granular} \mathbf{r}_{k0} \times m_k m_j \left(\frac{\boldsymbol{\sigma_i}}{\rho_i^2} + \frac{\boldsymbol{\sigma_j}}{\rho_j^2} - \Pi_{ij}\right)\nabla_i \mathbf{W_{ij}} \tag{3.25}$$

3.2.3   Regularizations

To reduce the oscillations in the stress field, the moving least square (MLS) method [32] has been applied to the kernel function. The stress and strain rate are calculated by using the reproducing kernel as follows:

$$\boldsymbol{\sigma}_i \;=\; \sum_j \frac{m_j}{\rho_j}\boldsymbol{\sigma}_j W_{ij}^{MLS} \tag{3.26}$$

$$\boldsymbol{\epsilon}_i \;=\; \sum_j \frac{m_j}{\rho_j}\boldsymbol{\epsilon}_j W_{ij}^{MLS} \tag{3.27}$$

46

Here, the reproducing kernel is defined as

$$W_{ij}^{MLS} = [\beta_0 + \beta_1(x_j - x_i) + \beta_2(x_j - x_i)^2]W_{ij} \tag{3.28}$$

The coefficients β_k is obtained by solving the following equations for each particle

$$[\beta_0, \beta_1, \beta_2]^T = A^{-1}[1, 0, 0]^T \tag{3.29}$$

where

$$A = \sum_j \frac{m_j}{\rho_j} \left\{ \begin{array}{ccc} 1 & (x_j - x_i) & (y_j - y_i) \\ (x_j - x_i) & (x_j - x_i)^2 & (x_j - x_i)(y_j - y_i) \\ (y_j - y_i) & (x_j - x_i)(y_j - y_i) & (y_j - y_i)^2 \end{array} \right\} W_{ij} \tag{3.30}$$

3.2.4 Boundary conditions

The fixed ghost particle boundary proposed in earlier work [62] has been adopted in this work to model the static wall (boundary) and robot appendage, as this formulation can be used to handle static, dynamic, and sharp edge boundary conditions well. The pressure at the boundary is derived from force balance at the wall:

$$p_w = \frac{\sum_f p_f W_{wf} + (\mathbf{g} - \mathbf{a}_w) \cdot \sum_f \rho_f \mathbf{x}_{wf} W_{wf}}{\sum_f W_{wf}} \tag{3.31}$$

The density of the wall is calculated from the equation of state

$$\rho_w = \rho_{0,j}\left(\frac{p_w - \chi}{p_{0,j}} + 1\right)^{\frac{1}{\gamma}} \tag{3.32}$$

Here, $\rho_{0,j}$ and $p_{0,j}$ are the reference density and the reference pressure of the interacting fluid particle j , and all the other parameters are defined according to earlier work [62].

3.2.5 Integration

For integrating the Newton's law of motion, the popular Verlet-Leapfrog algorithm is used. In adopting this approach, the field variables such as density, velocity vectors, and position vectors are updated at every time step as follows:

$$\rho_i^{n+1/2} = \rho_i^{n-1/2} + \Delta t \frac{D\rho_i}{Dt}^n \tag{3.33}$$

$$\mathbf{v}_i^{n+1/2} = \mathbf{v}_i^n + \frac{\Delta t}{2} \frac{D\mathbf{v}_i}{Dt}^n \tag{3.34}$$

$$\mathbf{x}_i^{n+1/2} = \mathbf{x}_i^n + \frac{\Delta t}{2} \mathbf{v}_i^{n+1/2} \tag{3.35}$$

The Courant-Friedrichs-Lewy condition is used to determine the time step to satisfy the following:

$$\Delta t \ \leq \ C_{cour}(\frac{h}{c_o})$$ (3.36)

Here, h is the smoothing length, c_o is the sound speed calculated by Eq. (3.16), and C_{cour} is the Courant coefficient.
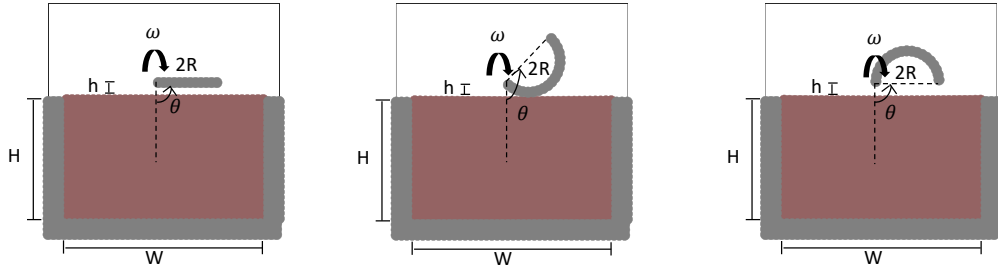
Figure 3.1:   Legs of different geometries (a) Flat leg, (b) C-leg, and (c) Reversed C-leg.

3.3   Results and Discussion

The case of interactions between a rigid robot leg and the granular material has been studied to test the proposed SPH framework.The motion of the rigid body is prescribed to be consistent with the experiment. It is a prototype of the legged robot. As this work is a first effort to explore the possible use of SPH method to investigate interactions between robots with granular terrain, the author has employed this simple test problem to build a foundation for future work.The dimension and other physical parameters of the robot legs (2R= 7.62cm, width=2.54cm, thick-
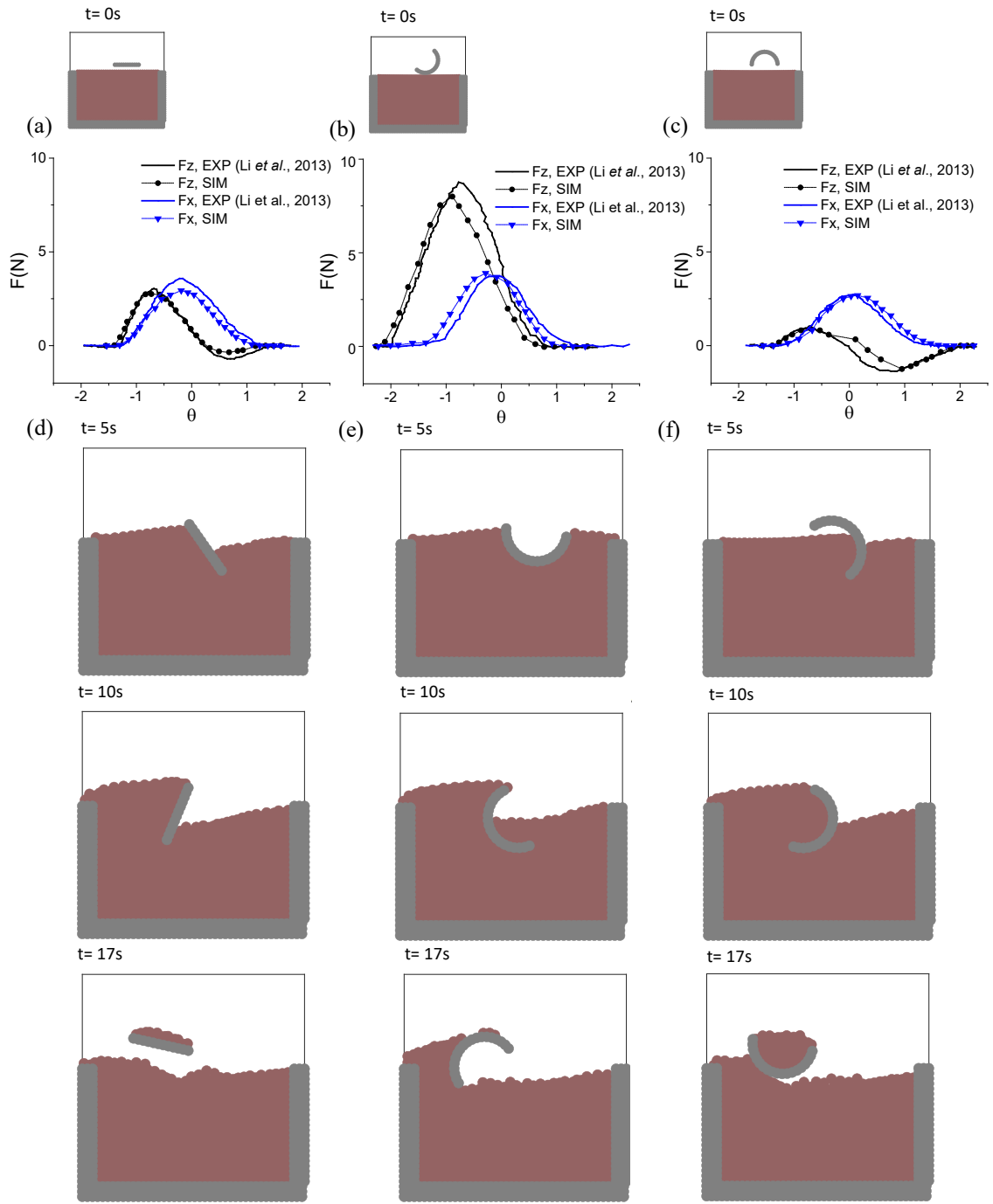
Figure 3.2: Validation of net lift Fz and thrust Fx versus leg angle θ for interactions of three leg models with 3mm closely packed glass spheres. The experimental results are from literature [48]: (a) Flat leg, (b) C-leg, (c) Reversed C-leg, (d) Profiles of flat leg at different time instants, (e) Profiles of C-leg at different time instants, and (f) Profiles of Reversed C-leg at different time instants.

50
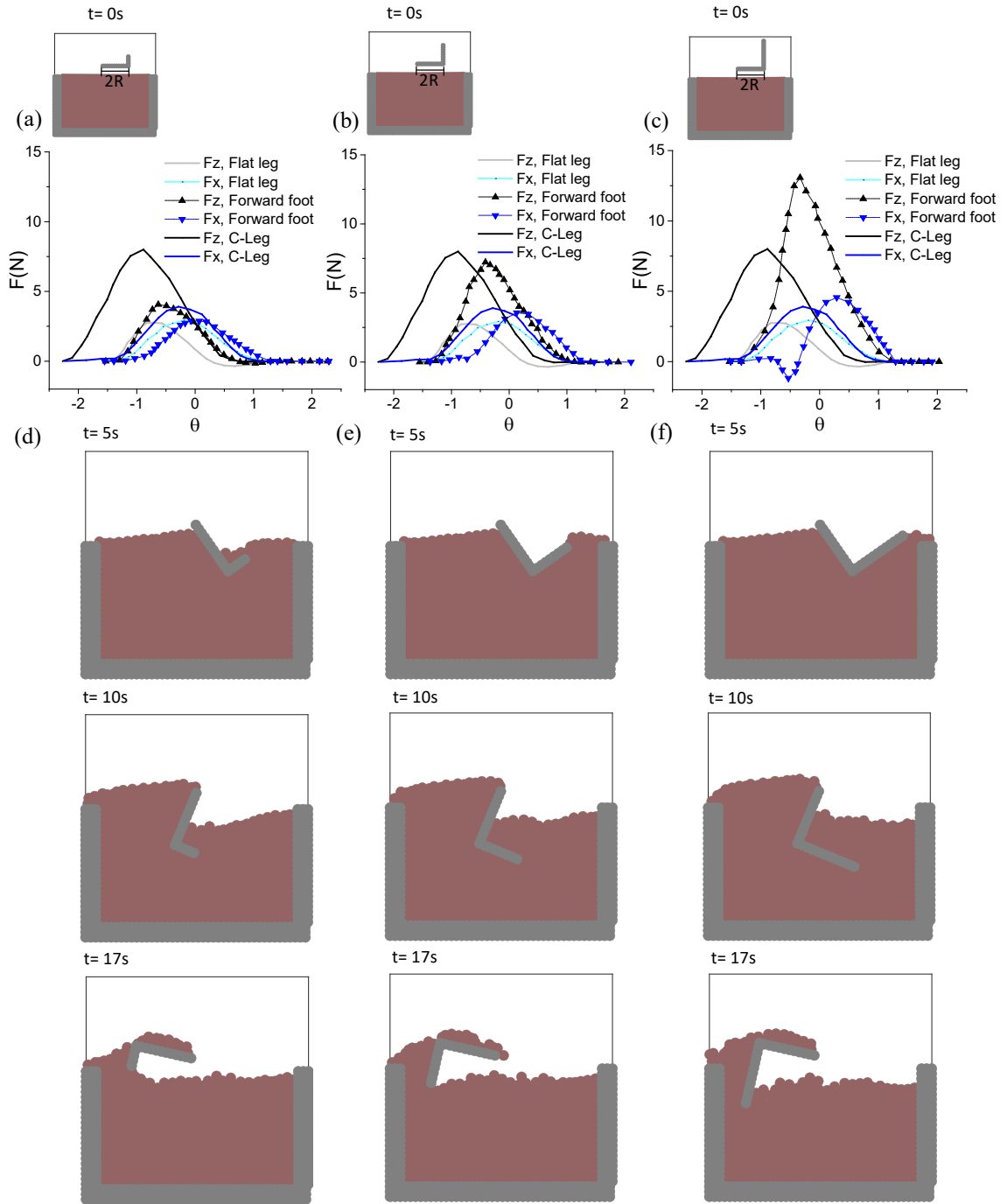
Figure 3.3: Comparison of net lift Fz and thrust Fx versus leg angle θ for flat leg, L- leg (leg with forward foot), and C-leg models: (a) L-leg, fl=0.33; (b) L-leg, fl=0.67; (c) L-leg, fl=1.00; (d) Profiles of L-leg, fl=0.33 at different time instants; (e) Profiles of L-leg, fl=0.67 at different time instants; and (f) Profiles of Reversed L-leg, fl=1.00 at different time instants.

51
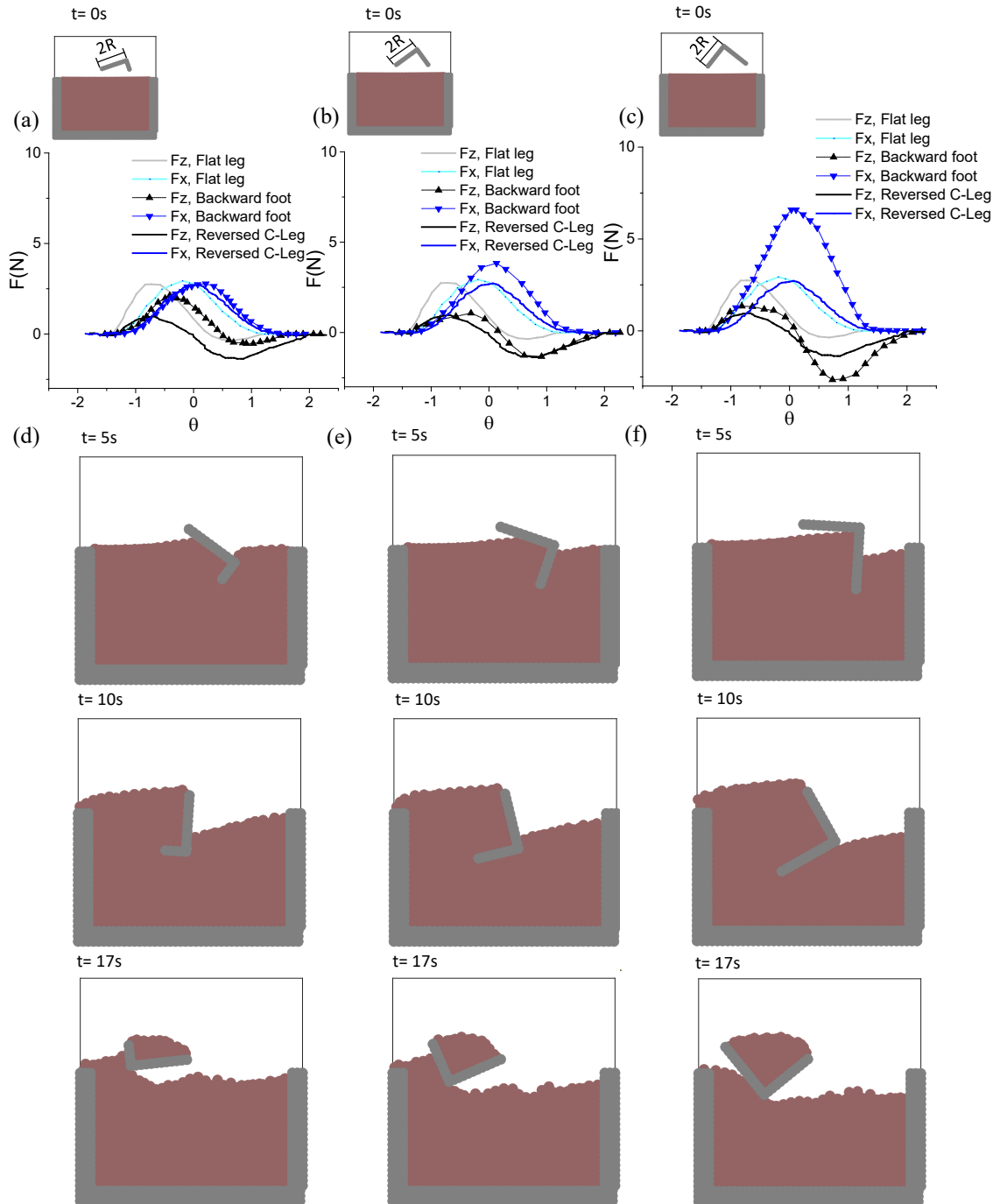
Figure 3.4: Comparison of net lift Fz and thrust Fx versus leg angle θ on flat leg, Reversed L- leg (leg with backward foot), and Reversed C-leg models: (a) Reversed L-leg, fl=0.33; (b) Reversed L-leg, fl=0.67; (c) Reversed L-leg, fl=1.00; (d) Profiles of Reversed L-leg, fl=0.33 at different time instants; (e) Profiles of Reversed L-leg, fl=0.67 at different time instants; and (f) Profiles of Reversed Reversed L-leg, fl=1.00 at different time instants.
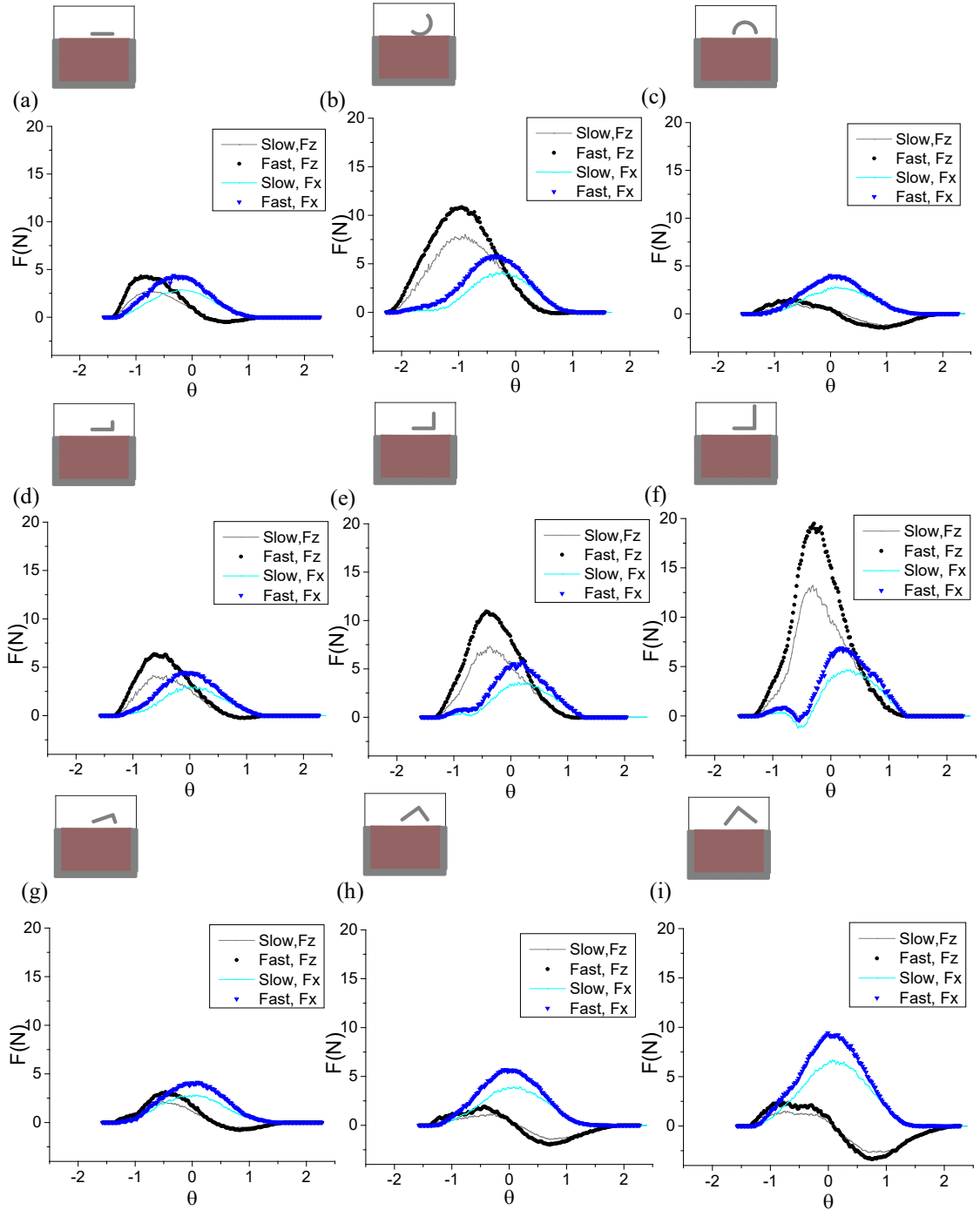
Figure 3.5: Comparison of net lift Fz and thrust Fx versus leg angle θ for fast and slow rotations: (a) Flat leg; (b) C-leg; (c) Reversed C-leg; (d) L-leg, fl=0.33; (e) L-leg, fl=0.67; (f) L-leg, fl=1.00; (g) Reversed L-leg, fl=0.33; (h) Reversed L-leg, fl=0.67; and (i) Reversed L-leg, fl=1.00.

ness=0.64cm) and granular bed (W=24cm, H=15cm deep) are the same as those reported in an earlier experimental study [48], as shown in Fig. 3.1. The granular media picked is 3 mm (diameter) glass spheres in a closely packed state with a particle material density of 2.6g/cm^3, volume fraction of 0.63, and angle of repose 23° ($\mu_1 = tan(23^o), \mu_2 = tan(33^o)$).

During the robot leg rotation simulation, the leg is first paused for 2 seconds, and then rotated clockwise with an angular velocity ω=0.2 rad/s at a hip height h=2cm within leg angle $-3\pi/4 \leq \theta \leq 3\pi/4$.

Overall, the results generated from the current computational framework are found to be consistent with experimental findings reported in the literature for robot legs with different geometries, as illustrated in Fig. 3.2. The advantage of continuum simulation over resistive force theory is the accuracy for curved C leg interaction with granular material. As reported in reference [48], the error of resistive forces for C-leg computed with resistive force theory is around 33%.While for continuum simulation, the error is less than 10% forthis case. And for legs of other shapes, the continuum simulation always yields more accurate results. In the simulations, only the contributions from granular particles in the container is considered for the computation of the resistive forces. The net lift force Fz and drag force Fx versus leg angle θ acting on flat leg, C-leg and reversed C-leg during interactions with 3mm closely packed glass spheres are shown in Fig. 3.2 (a), (b) and (c). Compared to a flat leg profile, the C-leg profile helps increase the net lift significantly, while with the reversed C-leg profile, one has the opposite situation due to the difference in the amount of granular material in the leg uplift. As the particles cannot penetrate the

54

legs, with the C-leg, one has more uplift of granular material than with a reversed C-leg when the leg rotates clockwise. However, there is not as much change in the net drag as that in the net lift with the three leg models because the movement of particles are bounded within the same boundary walls in the horizontal direction. The profiles of flat leg, C-leg and reversed C-leg at different time instants are shown in Fig. 3.2 (d), (e), and (f), which can serve as evidence of the amount of granular material the legs uplift.

Based on this validated model, the sensitive dependence of drag and lift forces on the length of the robot foot is investigated. The influence of forward foot with different lengths on the resistive forces is shown in Fig. 3.3. The length of the foot to leg ratio is defined as fl. In Fig. 3.3 (a), when fl is 0.33, it is shown that compared with a flat leg, the introduction of the forward foot increases the lift and drag forces because the forward foot uplifts more granular material. To generate the results shown in Fig. 3.3 (b), fl is set to 0.67. From a comparison between Fig. 3.3 (a) and Fig. 3.3 (b), one can infer that longer the foot is, the larger the lift and drag forces are. The resistive forces experienced by the L shaped legs are in between those obtained for the flat leg and C-leg. With regard to Fig. 3.3 (c), it is noted that if the length of the foot is increased continuously, then, the resulting lift and thrust forces exceed those of the C-leg as there is a sharp edge in the L shaped leg. The lift force is more sensitive than the drag force to the shape of the leg because of the different boundary conditions in the two directions. The granular particles are bounded by two fixed walls in the horizontal direction while in the vertical direction there is a fixed end and a free surface. In Fig.3.3 (d), (e), and (f), the profiles of

L-legs at different time instants are shown to help understand the change in the resistive forces.

In addition, the influence of backward foot with different lengths on the resistive forces is illustrated in Fig.3.4. In Fig.3.4 (a), when fl is 0.33, it is shown that compared with the flat leg, the introduction of backward foot increases drag force because more granular particles are pushed in the horizontal direction. However, with this geometry, one decreases the lift force because it is easier for the leg to intrude clockwisely into the granular material with a backward foot. From a comparison between Fig.3.4 (a) and Fig.3.4 (b), it is learned that the longer the foot is, the larger the lift and drag forces are. The lift forces of reversed L shaped legs are in between those obtained with the flat leg and reversed C-leg profiles. In Fig.3.4 (c), it is shown the drag force continues to increase if the length of the foot continues to increase. The lift force, however, stops decreasing and starts to increase. The lift force is less sensitive than the drag force to the shape of the leg. In Fig .3.4 (d), (e), and (f), the profiles of reverse L-legs at different time instants are shown to provide more details on the amount of granular particles different legs uplift to understand the changes in the resistive forces.

Finally, the influence of the angular velocity of legs on the resistive forces across different shapes is shown in Fig. 3.5. For all the cases, the angular velocity is 0.2rad/s for the slow rotation and 0.8rad/s for the fast rotation. For all of the leg shapes, the qualitative trend is the same; that is, the faster the leg rotates, the larger the thrust and lift forces are. Fr_{fast} is defined as the resistive forces in fast rotation and Fr_{slow} is used for the resistive forces in the slow rotation case. The

ratio $r_{fs} = Fr_{fast}/Fr_{slow}$ is slightly different in the horizontal and vertical directions across various leg shapes. This ratio r_{fs} is almost the same for all leg shapes. The lift force of C-leg is observed to be least sensitive to the increase of the rotation frequency of the legs and that of reversed C-leg is found to be the opposite due to the amount of granular material involved in the interaction.

3.4   Concluding Remarks

A computational framework based on the smoothed particle hydrodynamics (SPH) method has been developed for the investigation of single robot limb interaction with a granular substrate. The proposed SPH framework is validated by comparing numerical results obtained with this model with recent experimental findings and extended to study robot limbs across different shapes and stride frequencies. Compared with the flat leg, the C-leg is observed to increase the lift force significantly and the drag force a little, while with the reversed C-leg, one has the opposite situation due to the difference in the amount of granular material the leg uplift. Although the author could not carry out experimental validation for the simulations of flat legs with the forward and backward foot, the numerical findings can help understand the influence of foot on the leg locomotion on granular material. Compared with a flat leg, with the introduction of a forward foot, one increases the lift force because the forward foot helps uplift more granular material. The longer the foot, the larger the lift force. In contrast, the introduction of backward foot first decreases and then increases the lift force with the increase in the foot length.

The introduction of the foot always leads to an increase in the drag force. The drag forces experienced by legs with a backward foot are more sensitive than those experienced with a forward foot. The drag and lift forces increase with the increase of the angular velocity of the legs. The lift force experienced by a C-leg is found to be least sensitive to the increase in the rotation frequency of the legs and the trend with a reversed C-leg is the opposite. Through the current study, it is shown that the smoothed particle hydrodynamics method can be used to study the interactions of intruders with arbitrary geometry and granular material, and also be used to terra-mechanics problems where the interactions between the terrain and the body of interest are at small scales.

Chapter 4:   Hybrid Robot Motion on Particulate Soft Terrain

In this chapter, the legged and wheeled locomotion are combined to leverage the advantages of both locomotion modes, with the aim of having a resulting hybrid leg-wheel locomotion that can enable fast motion in any terrain condition. The previous experimentally validated computational framework for single robot appendage interaction with the granular system has been extended and coupled with a multibody simulator to model different robot configurations. Encouraging agreement is found amongst the numerical, theoretical, and experimental results, for a wide range of robot leg configurations, such as leg curvature and shape. The sensitive dependence of robot performance on different gaits has been investigated by parametric explorations.

The abovementioned physics-based simulation can serve as a high-fidelity tool to uncover clues about the underlying mechanism of dynamic interactions between robots and a soft terrain. However, real-time navigation in a challenging terrain requires fast prediction of the dynamic response of the robot, which is useful for terrain identification and robot gait adaption. Therefore, a data-driven modeling framework has also been developed for the fast estimation of the slippage and sinkage of robots. With the data-driven model, one can leverage the high-quality data

generated from the offline physics-based simulation for the training of a deep neural network founded on long short-term memory (LSTM) cells [70]. The results are expected to form a good basis for online robot navigation and exploration in unknown and complex terrains.

The rest of this chapter is organized into four sections to include the approach, results, and concluding remarks.

4.1 Approach

The physics-based modeling of hybrid robot motion on soft terrain has three components, which are the granular materials, whose model is the same that in reference in [58], two-way coupled interaction mechanism that is the same as that in earlier work [73], and the dynamics of the robot. The robot is treated as a rigid body composed of particles. Thus, the motion of the robot can be decomposed into the translational part and the rotational part. The equations of motion are written as shown next:

$$\frac{d\mathbf{r}_k}{dt} = \mathbf{u}_k \tag{4.1}$$

$$\mathbf{u}_k = \mathbf{U}_0 + \boldsymbol{\Omega}_0 \times \mathbf{r}_{k0} \tag{4.2}$$

$$\mathbf{a}_k = \frac{d\mathbf{U}_0}{dt} + \frac{d\boldsymbol{\Omega}_0}{dt} \times \mathbf{r}_{j0} + \boldsymbol{\Omega}_0 \times \mathbf{v}_{j0} \tag{4.3}$$

$$\frac{d\mathbf{U}_0}{dt} = \frac{\mathbf{F}_{granular-robot}}{M} + \mathbf{g} \tag{4.4}$$

$$\frac{d\mathbf{\Omega}_0}{dt} = \frac{\mathbf{T}_{granular-robot}}{I} \tag{4.5}$$

$$\mathbf{F}_{granular-robot} = \int_{\Gamma} \mathbf{n} \cdot \boldsymbol{\sigma} d\mathbf{x} \tag{4.6}$$

$$\mathbf{T}_{granular-robot} = \int_{\Gamma} \mathbf{r} \times (\mathbf{n} \cdot \boldsymbol{\sigma}) d\mathbf{x} \tag{4.7}$$

Sinkage and slipping are the two most important issues for robot mobility [71]. Wheel sinkage is regarded as the distance from the lowest point of the wheel in the soil to the horizontal flat terrain in relative research. Wheel slip occurs when the force applied to a wheel exceeds the traction available to that wheel. The force is applied to the wheel either longitudinally or laterally. Longitudinal force comes from the torque applied to the wheel by the engine or due to the brakes. It tends to either accelerate or decelerate the car. Lateral force is created when a vehicle is driven around a curve. It takes force to make a vehicle change direction. The tires and the ground provide lateral force. Slipping is defined as the following:

$$slip = \begin{cases} 1 - \dfrac{v_x}{R\omega} & \text{for} \quad v_x < R\omega \\[2ex] \dfrac{R\omega}{v_x} - 1 & \text{for} \quad v_x \geq R\omega \end{cases} \tag{4.8}$$

A positive slip indicates that the wheels are spinning; negative slip indicates that they are skidding.

A data-driven modeling framework has been developed for the fast estimation of the slippage and sinkage of robots. The data-driven model leverages the high-quality data generated from the offline physics-based simulation for the training of a deep neural network founded on long short-term memory (LSTM) cells [70]. The reason for choosing LSTM is because it is suitable for sequence modeling and can capture long term dependency. A single LSTM cell is shown in Fig. 4.1 and defined as:
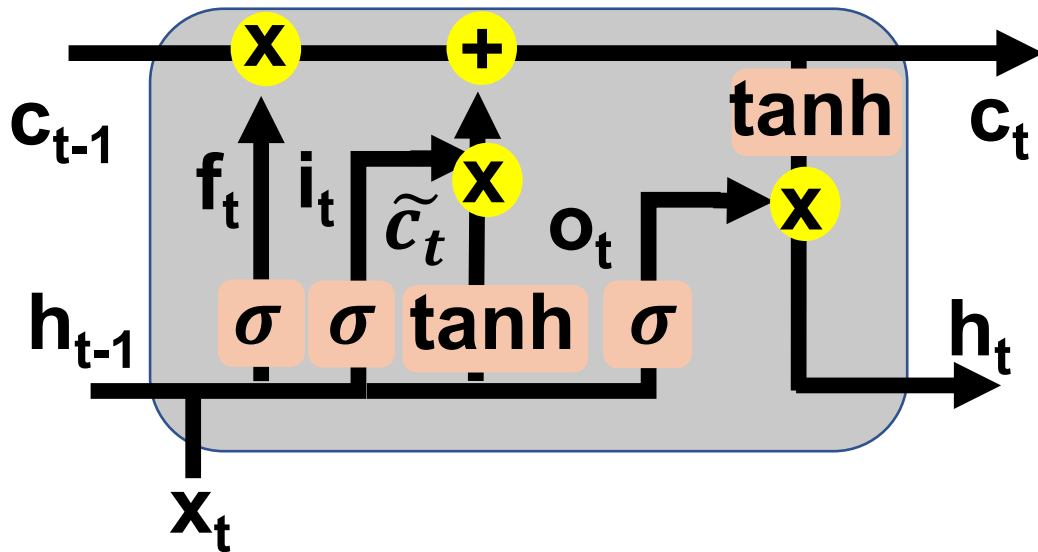
Figure 4.1:   LSTM cell

$$\mathbf{i}^{<t>} \;=\; \sigma(W_{ui}\mathbf{u}^{<t>} + W_{hi}\mathbf{h}^{<t-1>} + W_{ci}\mathbf{c}^{<t-1>} + \mathbf{b}_i) \tag{4.9}$$

$$\mathbf{f}^{<t>} \;=\; \sigma(W_{uf}\mathbf{u}^{<t>} + W_{hf}\mathbf{h}^{<t-1>} + W_{cf}\mathbf{c}^{<t-1>} + \mathbf{b}_f) \tag{4.10}$$

$$\mathbf{c}^{<t>} \;=\; \mathbf{f}^{<t>}\mathbf{c}^{<t-1>} + \mathbf{i}^{<t>} \circ tanh(W_{uc}\mathbf{u}^{<t>} + W_{hc}\mathbf{h}^{<t-1>} + \mathbf{b}_c) \tag{4.11}$$

$$\mathbf{o}^{<t>} \;=\; \sigma(W_{uo}\mathbf{u}^{<t>} + W_{ho}\mathbf{h}^{<t-1>} + W_{co}\mathbf{c}^{<t>} + \mathbf{b}_o) \tag{4.12}$$

$$\mathbf{h}^{<t>} \;=\; \mathbf{o}^{<t>} \circ tanh(\mathbf{c}^{<t>}) \tag{4.13}$$

wherein $\sigma(x) = 1/(1+e^{-x})$ is the sigmoid function, $\circ$ represents the Hadamard product, and $\mathbf{i}^{<t>}$, $\mathbf{f}^{<t>}$, $\mathbf{u}^{<t>}$, $\mathbf{c}^{<t>}$, and $\mathbf{h}^{<t>}$ are as defined the input gate, forget gate, update gate, cell memory, output gate, and cell hidden state at time step t. The weighting matrices are defined accordingly. The gradient is trapped in the cell and prevented from vanishing through the memory cell and controlling gates.

4.2 Results and Discussion

The wheel and legs across different morphologies are combined as designs of the hybrid locomotion system, which are shown in Figure. 4.2, such as the

Figure 4.2: Morphologies of hybrid wheels: (a) Flat-leg wheel, (b) C-leg wheel, (c) Reversed C-leg wheel, (d) L-leg wheel, and (e) Reversed L-leg wheel.

Figure 4.3: Hybrid wheel motion across morphologies: (a) Flat-leg wheel, (b) C-leg wheel, (c) Reversed C-leg wheel, (d) L-leg wheel, and (e) Reversed L-leg wheel.
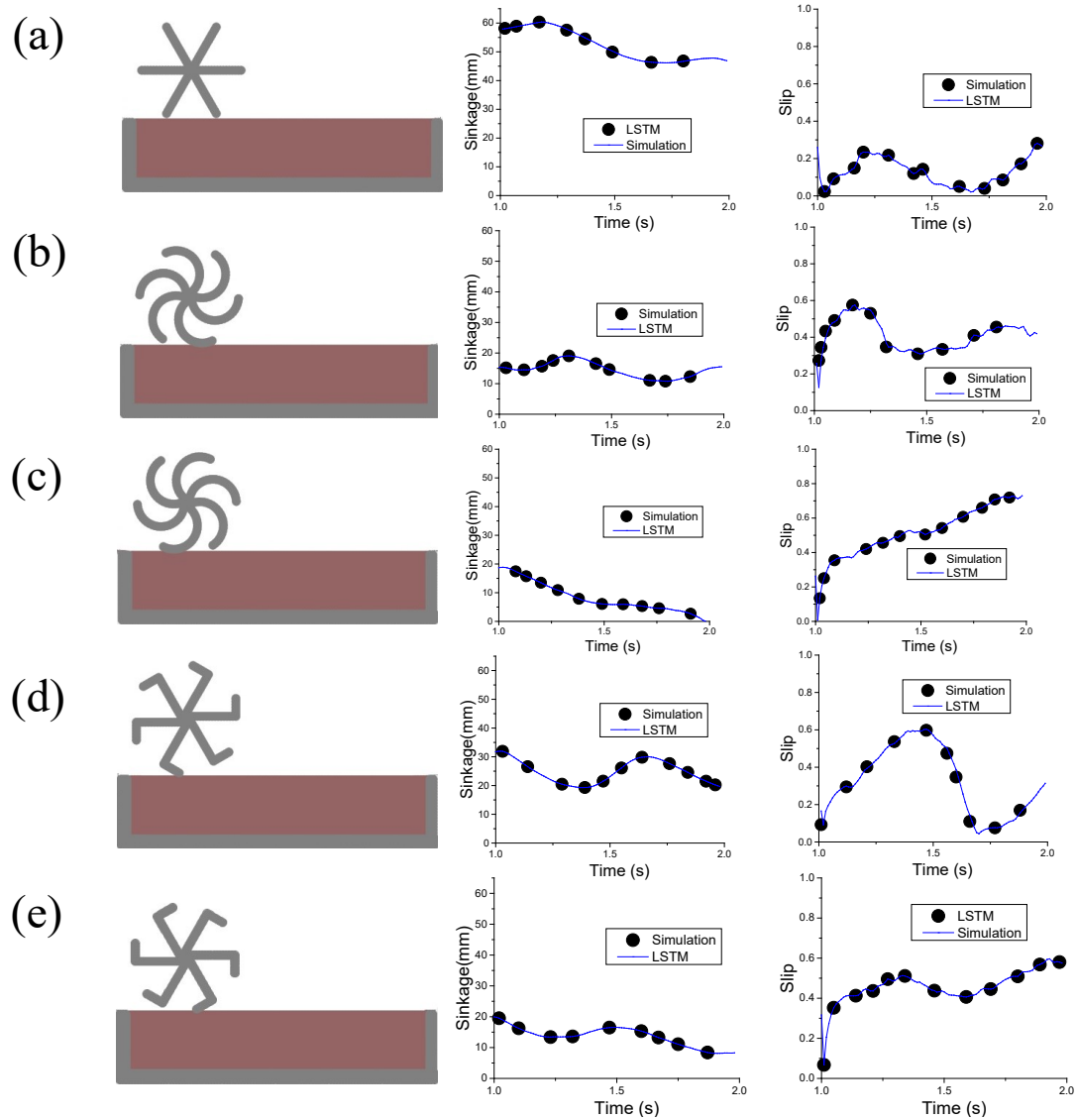
Figure 4.4: Sinkage and slip prediction with physics-based and LSTM prediction: (a) Flat-leg wheel, (b) C-leg wheel, (c) Reversed C-leg wheel, (d) L-leg wheel, and (e) Reversed L-leg wheel.

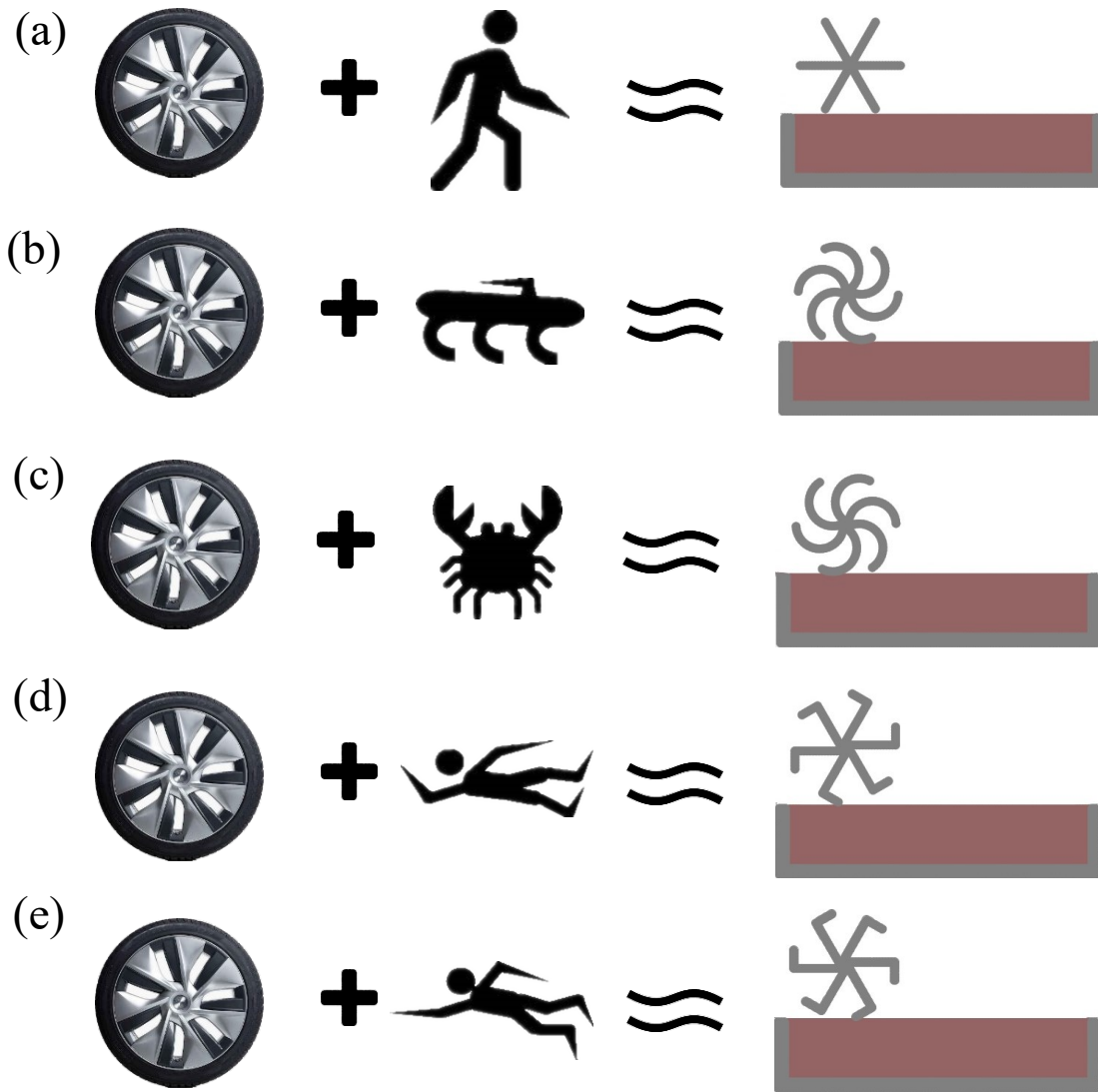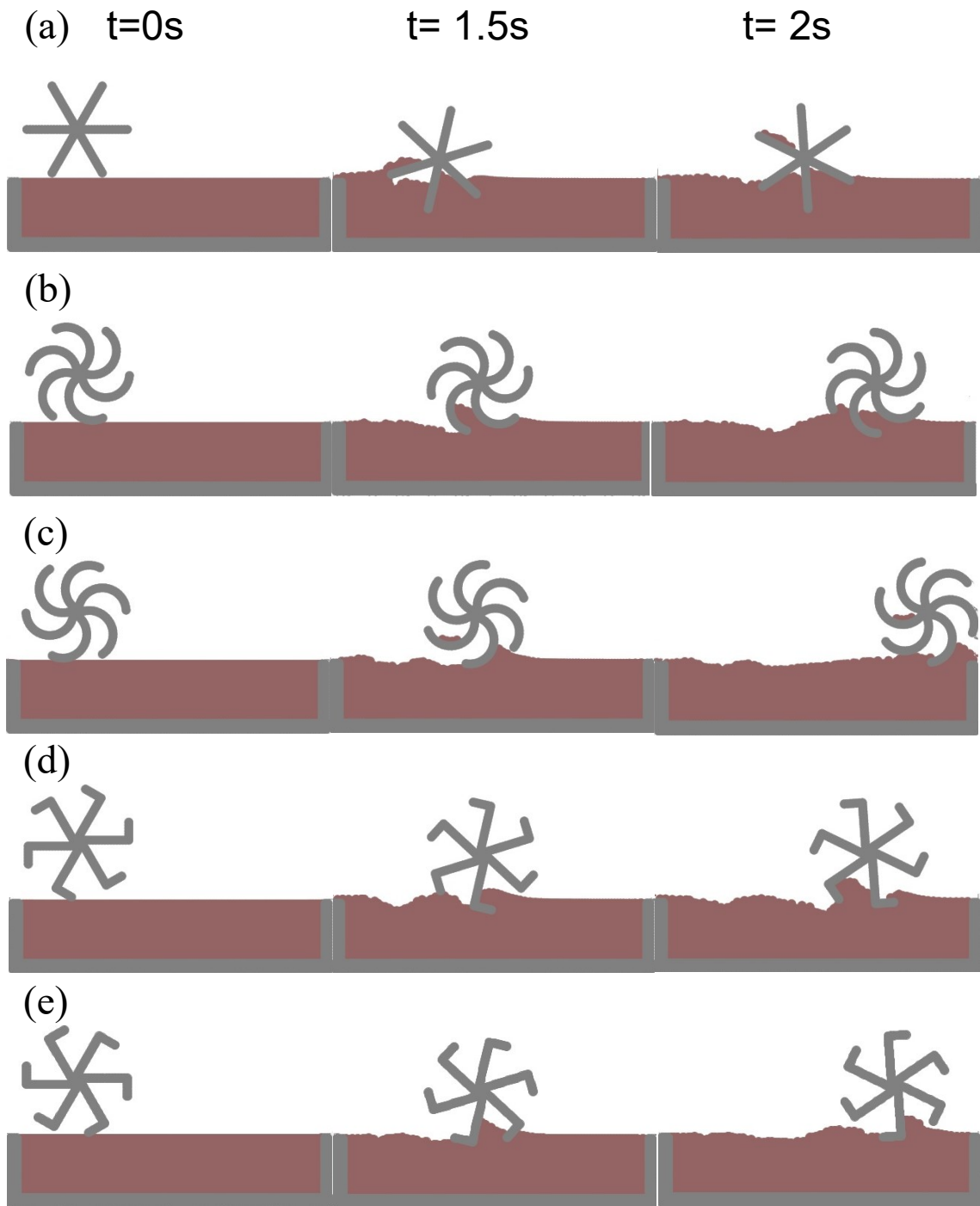flat-leg wheel, C-leg wheel, Reversed C-leg wheel, L-leg wheel, and Reversed L-leg wheel. The dimension and physical parameters are as follows: robot legs (2R= 8cm, width=10cm, thickness=0.5cm) and granular bed (W=50cm, H=10cm deep). The granular media picked is 3 mm (diameter) glass spheres in a closely packed state with a particle material density of 2.6g/cm^3, volume fraction of 0.63, and angle of repose 23° ($\mu_1 = tan(23^o), \mu_2 = tan(33^o)$). A physics-based computational framework has been developed by coupling robot dynamics and the previous computational framework for single robot appendage interaction with granular material. This newly developed framework is used to evaluate the mobility of hybrid robots.

From previousstudies (see for example, Chapter 3), a conclusion can be drawn that the resistive forces depend on the leg morphologies, stride frequency, and the load carries by the robots. To investigate the sensitive dependence of hybrid robot mobility on its morphologies, the stride frequency and carrying load are fixed for all of the simulation cases in Figure. 4.3. During the hybrid robot locomotion simulation, the leg-wheels are first paused for 2 seconds, and then rotated clockwise with an stride frequency ω=1.5 rad/s and a carrying load of 4.9N. One can tell from Figure. 4.3 that the proposed hybrid robots do not suffer from immobility issue on soft terrain like wheel locomotion because the legs can pull out themselves even when trapped in a terrain. The mobility of hybrid robots is influenced by their shapes. A flat-leg wheel has the worst mobility because of the large sinkage. Even if this Flat-leg wheel has the slowest speed, it dose not get trapped in sand. One just swims in the sand instead of walking on the sand. Reversed C-leg wheel in this case has the best mobility because the lift force is large enough to carry vertical load and

the drag force is small enough to resist motion.

A data-driven modeling framework has also been developed for the fast estimation of the slippage and sinkage of robots. Again, with this data-driven model, the author has leveraged the high-quality data generated from the offline physics-based simulation for the training of a deep neural network founded on long short-term memory (LSTM) cells. Both the physics-based and data-driven modeling approach can capture and predict the mobility of the hybrid robots.

4.3   Concluding Remarks

The legged and wheeled locomotion are combined to achieve fast mobility in any terrain condition. A physics-based computational framework has been developed to evaluate the mobility of hybrid robots. A data-driven modeling framework has also been developed for the fast estimation of the slippage and sinkage of robots. The proposed hybrid robots do not suffer from immobility issue on soft terrain like wheel locomotion because the legs can pull out themselves even when trapped in a terrain. The mobility of hybrid robots is influenced by their shapes. Reversed C leg-wheel in this case has the best mobility because the lift force is large enough to carry vertical load and the drag force is small enough to resist motion. Both the physics-based and data-driven modeling approaches can be used to capture the mobility of the hybrid robots.

Chapter 5:   Conclusion and Future Work

5.1   Summary

As described in previous chapters, the dissertation starts with the development of constitutive modeling to realistically describe complex behavior of a granular soft terrain. Then the newly developed model is numerically implemented and validated in a mesh-less SPH framework. The computational framework is then extended to study single robot appendage interaction with granular terrain. Finally, the legged and wheeled locomotion are combined to leverage the advantages of both locomotion modes aiming at the resulting hybrid leg-wheel locomotion can move fast in any terrain condition. The resulting hybrid leg-wheel locomotion is found to enable fast motion in any terrain condition. A data-driven modeling framework has also been developed for the fast estimation of the slippage and sinkage of robots.

Specifically, a constitutive model for both the dry and wet granular materials is implemented in a smoothed particle hydrodynamics framework to investigate the collapse of granular columns on flat and curved surfaces. The grain-scale capillary interaction is taken into consideration for capturing the behavior of wet granular materials. The proposed SPH framework is validated by comparing numerical results obtained with this model with recent experimental findings for dry and wet granular

column collapses on flat surfaces. Compared with dry granular materials, the introduction of surface tension in wet granular materials is noted to increase the shear stresses and enable a stronger structure with larger angles of repose. For collapses on curved surfaces, the differences in final profiles between wet granular materials and dry granular materials are not as pronounced as that on flat surfaces due to geometric constraints, although there is also an increase in internal shear strength. Through the current study, it is shown that the smoothed particle hydrodynamics method can be used to study wet granular materials.

In addition, a computational framework has been developed for the investigation of single robot limb interaction with a granular substrate. The proposed framework is validated by comparing numerical results obtained with this model with recent experimental findings and extended to study robot limbs across different shapes and stride frequencies. Compared with the flat leg, the C-leg is observed to increase the lift force significantly and the drag force a little, while the reversed C-leg does the opposite because of the difference in the amount of granular material the leg uplift. Compared with a flat leg, with the introduction of a forward foot, one increases the lift force because the forward foot helps uplift more granular material. The longer the foot, the larger the lift force. In contrast, the introduction of backward foot first decreases and then increases the lift force with the increase in the foot length. The introduction of the foot always leads to an increase in the drag force. The drag forces experienced by legs with a backward foot are more sensitive than those experienced with a forward foot. The drag and lift forces increase with the increase of the angular velocity of the legs. The lift force experienced by a C-leg

is found to be least sensitive to the increase in the rotation frequency of the legs and the trend with a reversed C-leg is the opposite. Through the current study, it is shown that the smoothed particle hydrodynamics method can be used to study the interactions of intruders with arbitrary geometry and granular material, and also be used to terra-mechanics problems where the interactions between the terrain and the body of interest are at small length scales.

Finally, the legged and wheeled locomotion are combined to achieve fast mobility in any terrain condition. A physics-based computational framework has been developed to evaluate the mobility of hybrid robots. A data-driven modeling framework has also been developed for the fast estimation of the slippage and sinkage of robots. The proposed hybrid robots do not suffer from immobility issue on soft terrain like wheel locomotion because the legs can pull out themselves even when trapped in a terrain. The mobility of hybrid robots is influenced by their shapes. Reversed C leg-wheel in this case has the best mobility because the lift force is large enough to carry vertical load and the drag force is small enough to resist motion. Both the physics-based and data-driven modeling approach can capture the mobility of the hybrid robots.

5.2   Suggestions for future work

In future studies, a few open questions worth exploring are as follows:

1. How can one transfer information at the micro-scale to the continuum scale model to bridge the gap between length scales for the unified modeling of granular

material?

2. Can one include multi-physics phenomena, such as thermal effect, size dependence, and level of water content in only one computational framework?

3. How can one leverage the combined benefit of high-fidelity simulation and computational efficient data-driven modeling approach for fast online prediction and control of robot navigation?

Besides the above questiosns, there are new opportunities of developing adaptive simulation tools for robot navigation in changing Arctic. The Arctic warms twice as fast as the rest of the world, which affects not only 4 million people living close to this region but also communities far from the Arctic. A warmer and increasing-accessible Arctic opens to the region to increasing research, navigation, and exploration, which will have a profound local and global influence. Navigation on natural terrains in the Arctic would help answer questions by observing the atmosphere above the ice: How much are the ice sheets shrinking? How fast is this change happening? Where is the ice melting the most? What factors are affecting these melts? These questions are essential to understand and predict changes in the Arctic environment. Unlike Antarctica where a polar climate dominates, the Arctic is more diverse. The special environment in the Arctic makes the motion on natural terrains in the Arctic quite complex. The evolving mapping and navigation techniques pave the way for robot operations in unmapped terrain like environments in the Arctic.

There has been significant progress made when it comes to robots perceiving and navigating their environments, like computer vision for mobile robot navigation.

Tundra　　　　　　Drift Ice

Solid Ice

Figure 5.1: Complex environment in Arctic [74]

Not much work has been done in numerical simulations, which are important to associate gait design and field test of robot locomotion on natural terrain in the Arctic, where complex contact and fluid-structure interaction occurs. The author's previous insight into conducting research on robot locomotion interaction with the granular substrate can be transferred to modeling the natural terrain in the Arctic. A plan is to refine and develop a three-dimensional walker simulator on natural terrain. Novel computational studies will be conducted on the multi-body robot that can perform hybrid-locomotion modes, such as walking, jumping, skating, climbing to adapt to complex terrains in the Arctic.

Figure 5.2: Cartoon of proposed numerical simulation of a robot navigating in the Arctic

Appendix A: Derivation of Hyperplastic Drucker-Prager Soil Model

To formulate the hyperplastic constitutive framework, one starts by defining the strain rate tensor,

$$\mathbf{D} \;=\; \frac{\dot{\mathbf{s}}}{2G} + \frac{1-2\nu}{3E}\dot{I}_1\delta_{ij} + \dot{\lambda}\frac{\partial g}{\partial \sigma} \tag{A.1}$$

From the definition of elastic bulk modulus K,

$$K = \frac{E}{3(1-2\nu)} \tag{A.2}$$

The strain rate tensor can be rewritten as

$$\mathbf{D} \;=\; \frac{\dot{\mathbf{s}}}{2G} + \frac{\dot{I}_1}{9K}\delta_{ij} + \dot{\lambda}\frac{\partial g}{\partial \sigma} \tag{A.3}$$

By definition of deviatoric stress tensor, one has

$$\dot{\mathbf{s}} \;=\; \dot{\sigma} - \frac{1}{3}\dot{I}_1\delta_{ij} \tag{A.4}$$

On substituting Eq.(A.4) into Eq.(A.3) and solving for $\dot{\sigma}$,

$$\dot{\sigma} \;=\; 2G\mathbf{D} - 2G\dot{\lambda} + \frac{3K-2G}{9k}\dot{I}_1\delta_{ij} \tag{A.5}$$

Taking the trace of both sides of Eq.(A.3) leads to

$$\dot{I}_1 \;=\; 3K(tr(\mathbf{D}) - tr(\dot{\lambda}\frac{\partial g}{\partial \sigma})) \tag{A.6}$$

After substituting Eq.(A.6) into Eq.(A.5), the generalized consitutive law for hyperplastic material can be derived as

$$\dot{\sigma} \;=\; 2G\dot{\mathbf{e}} - Ktr(\mathbf{D})\delta_{ij} - \dot{\lambda}[(K-\frac{2}{3}G)tr(\frac{\partial g}{\partial \sigma})\delta_{ij} + 2G\frac{\partial g}{\partial \sigma}] \tag{A.7}$$

where $\dot{e}$ is the deviatoric strain rate tensor defined as

$$\dot{\mathbf{e}} = \mathbf{D} - \frac{1}{3}tr(\mathbf{D})\delta_{ij} \tag{A.8}$$

For the Drucker-Prager material, the yield potential function $f(\sigma)$ and plastic potential function $g(\sigma)$ are given by

$$f(\sigma) = F(I_1, \sqrt{J_2}) - k_c \tag{A.9}$$

$$g(\sigma) = G(I_1, \sqrt{J_2}) - k_c \tag{A.10}$$

The derivation of these functions with respect to the Cauchy stress tensor can be derived by

$$\frac{\partial f}{\partial \sigma} = \frac{\partial f}{\partial I_1}\frac{\partial I_1}{\partial \sigma} + \frac{\partial f}{\partial \sqrt{J_2}}\frac{\partial \sqrt{J_2}}{\partial \sigma} = \frac{\partial f}{\partial I_1}\delta_{ij} + \frac{1}{2\sqrt{J_2}}\frac{\partial f}{\partial \sqrt{J_2}}\delta_{ij} \tag{A.11}$$

$$\frac{\partial g}{\partial \sigma} = \frac{\partial g}{\partial I_1}\frac{\partial I_1}{\partial \sigma} + \frac{\partial g}{\partial \sqrt{J_2}}\frac{\partial \sqrt{J_2}}{\partial \sigma} = \frac{\partial g}{\partial I_1}\delta_{ij} + \frac{1}{2\sqrt{J_2}}\frac{\partial g}{\partial \sqrt{J_2}}\delta_{ij} \tag{A.12}$$

After substituting Eq. (A.9) into Eq. (A.7), the generalized constitutive relationship for hyperplastic material with Drucker-Prager yield criterion can be obtained as,

$$\dot{\sigma} = 2G\dot{\mathbf{e}} - Ktr(\mathbf{D})\delta_{ij} - \dot{\lambda}[3K\frac{\partial g}{\partial I_1}\delta_{ij} + \frac{G}{\sqrt{J_2}}\frac{\partial g}{\partial \sqrt{J_2}}\mathbf{s}] \tag{A.13}$$

wherein the plastic multiplier can be derived by substituting Eq. (A.11) and Eq. (A.12) into its definition formula leading to

$$\dot{\lambda} = \frac{3Ktr(\mathbf{D})\dfrac{\partial f}{\partial I_1} + \dfrac{G}{\sqrt{J_2}}\dfrac{\partial f}{\partial \sqrt{J_2}}\mathbf{s} : \mathbf{D}}{9K\dfrac{\partial f}{\partial I_1}\dfrac{\partial g}{\partial I_1} + G\dfrac{\partial f}{\partial \sqrt{J_2}}\dfrac{\partial g}{\partial \sqrt{J_2}}} \tag{A.14}$$

Bibliography

[1] Yang, G.Z., Bellingham, J., Dupont, P.E., Fischer, P., Floridi, L., Full, R., Jacobstein, N., Kumar, V., McNutt, M., Merrifield, R. and Nelson, B.J. "The grand challenges of Science Robotics". Science robotics, **3**(14), p.eaar7650 (2018).

[2] Kennedy D, Norman C. "So much more to know". Science. **309**(5731):78-102 (2005).

[3] Gurtin, M.E., " An introduction to continuum mechanics". Academic press (1982).

[4] Kou, B., Cao, Y., Li, J., Xia, C., Li, Z., Dong, H., Zhang, A., Zhang, J., Kob, W., and Wang, Y. " Granular materials flow like complex fluids". Nature, **551**(7680), 360 (2017).

[5] Henann, D.L. and Kamrin, K. " A predictive, size-dependent continuum model for dense granular flows." Proceedings of the National Academy of Sciences, **110**(17), 6730-6735 (2013).

[6] Pouliquen, O. and Forterre, Y ."Friction law for dense granular flows: application to the motion of a mass down a rough inclined plane". Journal of fluid mechanics, **453**.133-151 (2002).

[7] Silbert, L.E., Erta, D., Grest, G.S., Halsey, T.C., Levine, D., and Plimpton, S.J."Granular flow down an inclined plane: Bagnold scaling and rheology". Physical Review E, **64**(5), 051302 (2001).

[8] Rognon, P.G., Roux, J.N., Naaim, M., and Chevoir, F."Dense flows of cohesive granular materials". Journal of Fluid Mechanics, **596**, 21-47, (2008).

[9] Ionescu, I.R., Mangeney, A., Bouchut, F., and Roche, O.”Viscoplastic modeling of granular column collapse with pressure-dependent rheology”. Journal of Non-Newtonian Fluid Mechanics, **219**,1-18, (2015).

[10] Lagrée, P.Y., Staron, L., and Popinet, S.”The granular column collapse as a continuum: validity of a two-dimensional NavierStokes model with a μ(I)-rheology”. Journal of Fluid Mechanics, **686**, 378-408, (2011).

[11] Campbell, C.S.”Rapid granular flows”. Annual Review of Fluid Mechanics, **22**(1), 57-90, (1990).

[12] MiDi, G.D.R.”On dense granular flows”. The European Physical Journal E, **14**(4),341-365, (2004).

[13] Artoni, R., Santomaso, A.C., Gabrieli, F., Tono, D., and Cola, S.”Collapse of quasi-two-dimensional wet granular columns”. Physical Review E, **87**(3), 032205, (2013).

[14] Mitarai, N. and Nori, F.”Wet granular materials”. Advances in Physics, **55**(1-2),1-45, (2006).

[15] Richefeu, V., El Youssoufi, M.S., and Radjai, F.”Shear strength properties of wet granular materials”. Physical Review E, **73**(5), 051304, (2006).

[16] Richefeu, V., El Youssoufi, M.S., Peyroux, R. and Radjai, F. ”A model of capillary cohesion for numerical simulations of 3D polydisperse granular media”. International Journal for Numerical and Analytical Methods in Geomechanics,**32**(11), 1365-1383, (2008).

[17] Wang, J.P., Gallo, E., Franois, B., Gabrieli, F. and Lambert, P. Capillary force and rupture of funicular liquid bridges between three spherical bodies. Powder Technology, **305**, 89-98, (2017).

[18] Samadani, A. and Kudrolli, A.”Angle of repose and segregation in cohesive granular matter”. Physical Review E, **64**(5), 051301, (2001).

[19] Jop, P., Forterre, Y., and Pouliquen, O.”A constitutive law for dense granular flows”. Nature, **441**(7094), 727, (2006).

[20] Chambon, G., Bouvarel, R., Laigle, D. and Naaim, M.”Numerical simulations of granular free-surface flows using smoothed particle hydrodynamics”. Journal of Non-Newtonian Fluid Mechanics, **166**(12-13), 698-712, (2011).

[21] Kamrin, K. and Koval, G."Nonlocal constitutive relation for steady granular flow". Physical Review Letters, **108**(17), 178301, (2012).

[22] Da-Cruz, F., Emam, S., Prochnow, M., Roux, J.N., and Chevoir, F."Rheophysics of dense granular materials: Discrete simulation of plane shear flows". Physical Review E, **72**(2), 021309, (2005).

[23] Gabrieli, F., Artoni, R., Santomaso, A., and Cola, S."Discrete particle simulations and experiments on the collapse of wet granular columns". Physics of fluids, **25**(10), 103303, (2013).

[24] Staron, L. and Hinch, E.J."Study of the collapse of granular columns using two-dimensional discrete-grain simulation". Journal of Fluid Mechanics, **545**, 1-27, (2005).

[25] Guo, N. and Zhao, J." A coupled FEM/DEM approach for hierarchical multiscale modelling of granular media". International Journal for Numerical Methods in Engineering, **99**(11), 789-818, (2014).

[26] Dunatunga, S., March."Simulation of granular flows through their many phases". In APS Meeting Abstracts, (2015).

[27] Hurley, R.C. and Andrade, J.E."Continuum modeling of rate-dependent granular flows in SPH". Computational Particle Mechanics, **4**(1), pp.119-130, (2017).

[28] Bui, H.H., Fukagawa, R., Sako, K., and Ohno, S."Lagrangian meshfree particles method (SPH) for large deformation and failure flows of geomaterial using elasticplastic soil constitutive model". International Journal for Numerical and Analytical Methods in Geomechanics, **32**(12), 1537-1570, (2008).

[29] Chen, W. and Qiu, T."Numerical simulations for large deformation of granular materials using smoothed particle hydrodynamics method". International Journal of Geomechanics, **12**(2), pp.127-135, (2011).

[30] Minatti, L. and Paris, E."A SPH model for the simulation of free surface granular flows in a dense regime". Applied Mathematical Modelling, **39**(1), 363-382, (2015).

[31] Peng, C., Guo, X., Wu, W., and Wang, Y. "Unified modelling of granular media with Smoothed Particle Hydrodynamics". Acta Geotechnica, **11**(6), 1231-1247, (2016).

[32] Nguyen, C.T., Nguyen, C.T., Bui, H.H., Nguyen, G.D., and Fukagawa, R."A new SPH-based approach to simulation of granular flows using viscous damping and stress regularisation". Landslides, **14**(1), 69-81, (2017).

[33] Szewc, K."Smoothed particle hydrodynamics modeling of granular column collapse". Granular Matter, **19**(1), 3, (2017).

[34] Liu, G.R. and Liu, M.B. *Smoothed particle hydrodynamics: a meshfree particle method.* (World Scientific, 2003).

[35] Monaghan, J.J."Simulating free surface flows with SPH". Journal of computational physics, **110**(2), 399-406, (1994).

[36] Chabalko, C. and Balachandran, B."GPU based simulation of physical systems characterized by mobile discrete interactions". In Developments in Parallel, Distributed, Grid, and Cloud Computing in Engineering, 95-124, Saxe-Coburg Publications, (2013).

[37] Morris, J.P., Fox, P.J., and Zhu, Y."Modeling low Reynolds number incompressible flows using SPH". Journal of computational Physics, **136**(1), 214-226, (1997).

[38] Wang, G., Riaz, A., and Balachandran, B."Computational studies on interactions between robot leg and deformable terrain". In Proceedia Engineering, **199**, 2439-2444, (2017).

[39] Korzani, M.G., Galindo-Torres, S.A., Scheuermann, A. and Williams, D.J. "SPH approach for simulating hydro-mechanical processes with large deformations and variable permeabilities". Acta Geotechnica, **13**(2), 303-316, (2018).

[40] Neto, A.H.F. and Borja, R.I. "Continuum hydrodynamics of dry granular flows employing multiplicative elastoplasticity". Acta Geotechnica, **13**(5), 1027-1040, (2018).

[41] Kermani, E. and Qiu, T. "Simulation of quasi-static axisymmetric collapse of granular columns using smoothed particle hydrodynamics and discrete element methods". Acta Geotechnica, 1-15, (2018).

[42] Marrone, S., Antuono, M., Colagrossi, A., Colicchio, G., Le Touz, D., and Graziani, G."δ-SPH model for simulating violent impact flows". Computer Methods in Applied Mechanics and Engineering, **200**(13-16),1526-1542, (2011).

[43] Knepper, W.A. ed. *Agglomeration.* (Interscience Publishers, 1962).

[44] Monaghan, J.J. "SPH without a tensile instability". Journal of Computational Physics, **159**(2), 290-311, (2000).

[45] Gabrieli, F., Artoni, R., Santomaso, A. and Cola, S. "Discrete particle simulations and experiments on the collapse of wet granular columns". Physics of Fluids, **25**(10), 103303, (2013).

[46] Dehnen, W. and Aly, H. "Improving convergence in smoothed particle hydrodynamics simulations without pairing instability". Monthly Notices of the Royal Astronomical Society, **425**(2), pp.1068-1082, (2012).

[47] Mao, Z., Liu, G.R. and Dong, X. "A comprehensive study on the parameters setting in smoothed particle hydrodynamics (SPH) method applied to hydrodynamics problems". Computers and Geotechnics, **92**, 77-95, (2017).

[48] Li, C., Zhang, T. and Goldman, D.I."A terradynamics of legged locomotion on granular media". science, **339**(6126),1408-1412, (2013).

[49] Lee, D., Kim, G., Kim, D., Myung, H. and Choi, H.T. "Vision-based object detection and tracking for autonomous navigation of underwater robots". Ocean Engineering, **48**, 59-68, (2012).

[50] Cabrera, F.J.C. "In-situ soil sensing for planetary micro-rovers with hybrid wheel-leg systems." University of Surrey ,United Kingdom, (2016).

[51] Li, C., Umbanhowar, P.B., Komsuoglu, H., Koditschek, D.E. and Goldman, D.I. "Sensitive dependence of the motion of a legged robot on granular media". Proceedings of the National Academy of Sciences, **106**(9), 3029-3034, (2009).

[52] Ding, L., Gao, H., Deng, Z., Nagatani, K. and Yoshida, K. "Experimental study and analysis on driving wheels performance for planetary exploration rovers moving in deformable soil". Journal of Terramechanics, **48**(1), 27-45, (2011).

[53] Bekker, M.G. *Introduction to terrain-vehicle systems*, (1969).

[54] Ding, L., Nagatani, K., Sato, K., Mora, A., Yoshida, K., Gao, H. and Deng, Z. Terramechanics-based high-fidelity dynamics simulation for wheeled mobile robot on deformable rough terrain. In 2010 IEEE International Conference on Robotics and Automation, 4922-4927. IEEE, (2010).

[55] Li, C., Zhang, T. and Goldman, D.I. A resistive force model for legged locomotion on granular media. In Adaptive Mobile Robotics , 433-440, (2012).

[56] Plagemann, C., Mischke, S., Prentice, S., Kersting, K., Roy, N. and Burgard, Wr. Learning predictive terrain models for legged robot locomotion. In 2008 IEEE/RSJ International Conference on Intelligent Robots and Systems ,3545-3552. IEEE, (2008).

[57] Agarwal, S., Senatore, C., Zhang, T., Kingsbury, M., Iagnemma, K., Goldman, D.I. and Kamrin, K. Modeling of the interaction of rigid wheels with dry granular media. Journal of Terramechanics, **85**, 1-14, (2019).

[58] Wang, G., Riaz, A. and Balachandran, B. Smooth particle hydrodynamics studies of wet granular column collapses. Acta Geotechnica, **15**, 1205–1217, (2020).

[59] Fern, E.J. and Soga, K. The role of constitutive models in MPM simulations of granular column collapses. Acta Geotechnica, **11**(3), 659-678, (2016).

[60] Takahashi, T., Dobashi, Y., Fujishiro, I., Nishita, T. and Lin, M.C. Implicit formulation for SPHbased viscous fluids. In Computer Graphics Forum,**34**(2), 493-502, (2015).

[61] MiDi, G.D.R. On dense granular flows. The European Physical Journal E, **14**(4), 341-365, (2004).

[62] Adami, S., Hu, X.Y. and Adams, N.A. A generalized wall boundary condition for smoothed particle hydrodynamics. Journal of Computational Physics, **231**(21), 7057-7075, (2012).

[63] Meirion-Griffith, G. and Spenko, M. "A modified pressuresinkage model for small, rigid wheels on deformable terrains". Journal of Terramechanics, **48**(2),149-155, (2011).

[64] Kermani, E. and Qiu, T. Simulation of quasi-static axisymmetric collapse of granular columns using smoothed particle hydrodynamics and discrete element methods. Acta Geotechnica, pp.1-15, 2018.

[65] Aguilar, J. and Goldman, D.I."Robophysical study of jumping dynamics on granular media". Nature Physics, **12**(3), 278, (2016).

[66] Marvi, H., Gong, C., Gravish, N., Astley, H., Travers, M., Hatton, R.L., Mendelson, J.R., Choset, H., Hu, D.L. and Goldman, D.I."Sidewinding with minimal slip: Snake and robot ascent of sandy slopes". Science, **346**(6206), 224-229, (2014).

[67] Senatore, C. and Iagnemma, K."Analysis of stress distributions under lightweight wheeled vehicles". Journal of Terramechanics, **51**, 1-17, (2014).

[68] Ding, L., Nagatani, K., Sato, K., Mora, A., Yoshida, K., Gao, H. and Deng, Z. "Terramechanics-based high-fidelity dynamics simulation for wheeled mobile robot on deformable rough terrain". In Robotics and Automation (ICRA), IEEE International Conference, 4922-4927, (2010).

[69] Peng, C., Guo, X., Wu, W., and Wang, Y. "Unified modelling of granular media with Smoothed Particle Hydrodynamics". Acta Geotechnica, **11**(6), 1231-1247, (2016).

[70] Hochreiter, S. and Schmidhuber, J. "Long short-term memory". Neural computation, **9**(8), 1735-1780, (1997).

[71] Iagnemma, K., Kang, S., Shibly, H. and Dubowsky, S., 2004. Online terrain parameter estimation for wheeled mobile robots with application to planetary rovers. IEEE transactions on robotics, 20(5), pp.921-927.

[72] Askari, H. and Kamrin, K. "Intrusion rheology in grains and other flowable materials". Nature materials, **15**(12),1274, (2016).

[73] Wang, G., Riaz, A. and Balachandran, B. Continuum Modeling and Simulation of Robotic Appendage Interaction with Granular Material. ASME Journal of Applied Mechanics. (2021, Accepted).

[74] Lewkowicz, A.G. and Way, R.G., 2019. Extremes of summer climate trigger thousands of thermokarst landslides in a High Arctic environment. Nature communications, 10(1), pp.1-11.